nature photonics

Article

https://doi.org/10.1038/s41566-023-01250-9

A Purcell-enabled monolayer semiconductor free-space optical modulator

Received: 26 February 2023

Accepted: 8 June 2023

Published online: 17 July 2023

Check for updates

Qitong Li[1], Jung-Hwan Song[1,6], Fenghao Xu[1,6], Jorik van de Groep[1,2,6], Jiho Hong[1], Alwin Daus[3], Yan Joe Lee[1], Amalya C. Johnson[4], Eric Pop[3], Fang Liu[5] & Mark L. Brongersma[1]

Dephasing and non-radiative decay processes limit the performance of a wide variety of quantum devices at room temperature. Here we illustrate a general pathway to notably reduce the detrimental impact of these undesired effects through photonic design of the device electrodes. Our design facilitates a large Purcell enhancement that speeds up competing, desired radiative decay while also enabling convenient electrical gating and charge injection functions. We demonstrate the concept with a free-space optical modulator based on an atomically thin semiconductor. By engineering the plasmonic response of a nanopatterned silver gate pad, we successfully enhance the radiative decay rate of excitons in a tungsten disulfide monolayer by one order of magnitude to create record-high modulation efficiencies for this class of materials at room temperature. We experimentally observe a 10% reflectance change as well as 3 dB signal modulation, corresponding to a 20-fold enhancement compared with modulation using a suspended monolayer in vacuum. We also illustrate how dynamic control of light fields can be achieved with designer surface patterns. This research highlights the benefits of applying radiative decay engineering as a powerful tool in creating high-performance devices that complements substantial efforts to improve the quality of materials.

Transition metal dichalcogenide (TMDC) monolayers display an impressive set of electronic and optical properties. Most notably, they can serve as direct band gap emitters[1,2] that can offer high quantum yields[3] and a broad tunability of the sheet conductivity[4]. For these reasons, they are now actively explored as a new materials platform for next-generation low-dimensional electronics[5] and optoelectronics[6,7], and provide an exciting playground to study quantum and correlated electron physics[8]. For nanophotonic applications, the very strong and tunable light–matter interaction enabled by excitons is particularly attractive[9–13]. In contrast to many bulk semiconductors and even quantum wells, excitons in TMDC monolayers survive at room temperature as a reduced dielectric screening, and enhanced quantum confinement in these atomically thin layers yield exciton binding energies as high as a few hundreds of millielectron volts[14]. The large electrical tunability of exciton resonances[15] comes with an exciting prospect to efficiently modulate[16] and dynamically control light fields with low switching energies[17,18]. Such dynamic control can find a wide range of emerging applications, including free-space optical communications[19], optical phased arrays[20], image processing[21] and optical neural networks[22]. These applications are hard to achieve in compact devices that employ conventional semiconductors and noble metals, as they only exhibit weak electro-refractive and electro-absorptive effects[23,24]. Two-dimensional (2D) semiconductors therefore seem very promising, but unfortunately their exciton resonances do severely weaken and

[1]Geballe Laboratory for Advanced Materials, Stanford University, Stanford, CA, USA. [2]Van der Waals–Zeeman Institute for Experimental Physics, Institute of Physics, University of Amsterdam, Amsterdam, the Netherlands. [3]Department of Electrical Engineering, Stanford University, Stanford, CA, USA. [4]Department of Materials Science and Engineering, Stanford University, Stanford, CA, USA. [5]Department of Chemistry, Stanford University, Stanford, CA, USA. [6]These authors contributed equally: Jung-Hwan Song, Fenghao Xu, Jorik van de Groep. e-mail: brongersma@stanford.edu

https://doi.org/10.1038/s41566-023-01250-9

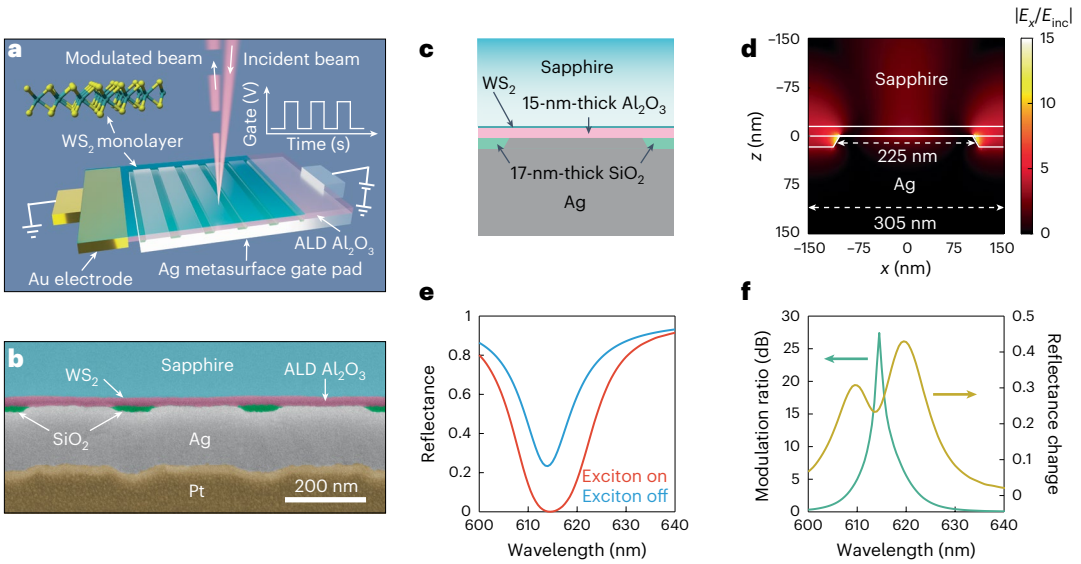

Fig. 1 | Monolayer WS_2 free-space optical modulator. a, Schematic of a monolayer WS_2 free-space optical modulator based on a MOS capacitor configuration. The intensity of the reflected beam is modulated by varying the gate voltage between the gold electrode and the silver metasurface gate pad. **b**, Cross-sectional scanning electron microscope (SEM) image of the fabricated optical modulator. A false-colour overlay is used to enhance the contrast between different layers in the device. Scale bar, 200 nm. **c**,**d**, Detailed cross-sectional geometry (**c**) and the simulated corresponding electric field distribution (**d**) of the designed optical modulator in one period under transverse-magnetic-polarized normal illumination. E_x is the simulated electric field in x direction, and E_{inc} is the amplitude of the incident field. The incident wavelength is 615 nm. **e**, Simulated reflection spectra of the designed optical modulator under transverse-magnetic-polarized illumination at normal incidence. The exciton resonance in the WS_2 monolayer is switched on (red) and off (blue) artificially by first separating the exciton resonance contribution from the dielectric background in the dielectric function of the WS_2 monolayer and then keeping (on-state) or removing (off-state) this contribution in the dielectric function. **f**, Extracted modulation ratio (green) and absolute reflectance change (yellow) of the designed optical modulator from the simulations in **e**.

broaden with increasing temperature and it is a huge challenge to find ways to harness them effectively at room temperature.

The reported near-unity reflection modulation with TMDC monolayers at cryogenic temperatures[25,26] essentially disappears at room temperature, and only a reflection modulation of ~0.5% has been achieved so far[17]. This occurs because the non-radiative decay and dephasing rates of excitons increase to a value that is about one order of magnitude larger than their intrinsic radiative decay rates in vacuum at ~300 K (refs. 26–29). Challenges with non-radiative decay and dephasing are common to a wide range of quantum materials and they preclude their use in devices operating at room temperature. Researchers usually attempt to limit these undesired processes by improving the materials' quality, but photonic engineering brings an equally powerful route to overcome this challenge. For example, in plasmonics it is well-established that deep-subwavelength-sized metal nanoparticles are plagued by very low scattering efficiencies. This is because the ratio of the radiative and non-radiative decay rates for their surface plasmon excitations is similar in magnitude to those seen in TMDC monolayers at room temperature[26,30]. Here, superradiance effects were successfully engineered to enhance their scattering intensities[31,32]. It was also recently suggested that radiative decay engineering can resolve issues with dephasing of quantum emitters[33,34]. Now we show that 2D semiconductors can be used effectively to electro-optically modulate light waves at room temperature by speeding up their radiative decay[35]. We place WS_2 monolayers on nanostructured metallic substrates that support surface plasmon excitations capable of enhancing the radiative decay rate of coherently excited excitons via the Purcell effect by one order of magnitude. These photonic substrates can perform a dual function as a low-quality factor (Q) cavity and a high-conductivity gate pad for low-power, solid-state electrical tuning of the excitonic resonance. We further demonstrate dynamic light-field control by adopting a different metasurface gate pad design to electrically modulate the intensity of a steered optical beam.

Results

Concept of a monolayer WS_2 free-space optical modulator

Figure 1a shows a schematic of the designed monolayer tungsten disulfide (WS_2) free-space optical modulator. A piece of WS_2 monolayer is electrically connected to a gold electrode and placed on top of a nanopatterned silver gate pad spaced by a 15-nm-thick Al_2O_3 gate oxide, forming a metal–oxide–semiconductor (MOS) capacitor. The topography of the silver gate pad is defined by a 17-nm-thick SiO_2 nano-strip array with a period (p) of 305 nm (Fig. 1b). The detailed cross-sectional geometry for one period of the designed modulator is displayed in Fig. 1c. To analyse its behaviour in optical simulations, we first perform ellipsometry to quantify the optical properties of the various materials in the device (see Methods). By using ellipsometric data for WS_2, it is assumed that this material can be treated as spatially uniform and that its optical behaviour can be modelled with a linear, coherent response. This is a frequently made assumption that can provide many valuable insights, although it tacitly assumes that the exciton broadening can fully be ascribed to non-radiative decay. For an illumination wavelength of 615 nm, we can see that the simulated electric field near the metal surface is greatly enhanced (Fig. 1d) and this is key to achieving efficient optical modulation. The situation is very different from a conventional MOS configuration with planar metallic gate pads. Such gate pads display severely weakened electric fields near their surface due to the approximately π reflection phase pickup for incident light waves (Supplementary Fig. 1). To electrically modulate the device, we capitalize on the demonstrated possibility to fully switch exciton resonances in a WS_2 monolayer on and off by charge injection[9,15,17]. Under the assumption that this can also be accomplished in our device (Supplementary Fig. 2), we quantify the achievable modulation from wave-optics simulations (Fig. 1e). A more than 25 dB modulation ratio and a 40% reflectance change are observed in the simulation upon switching of the exciton resonance (Fig. 1f). The nanopatterned gate pad thus provides a large boost in the reflection modulation by almost two orders of magnitude

https://doi.org/10.1038/s41566-023-01250-9

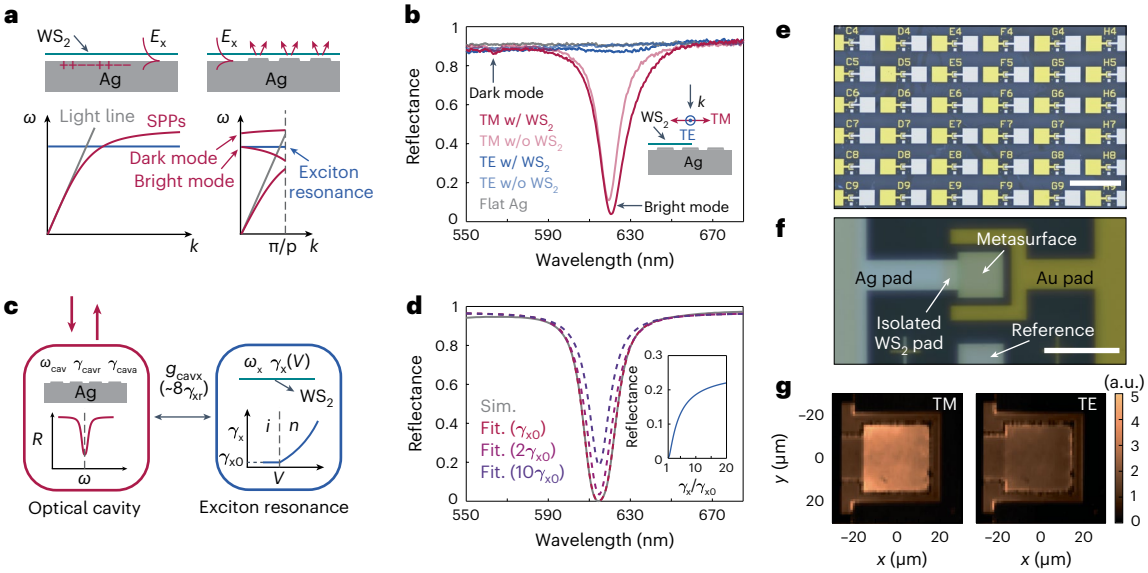

Fig. 2 | Enhanced modulation with an silver metasurface gate pad. a, Realization of a quasi-guided SPP mode supported by the metasurface gate pad following the introduction of a periodic perturbation to the top surface of the silver gate pad. Red curves represent the modal dispersion of the (perturbed) SPPs at the silver/dielectric interface, and grey lines refer to the light lines in the dielectric. Two optical modes are found at the Γ-point near the exciton resonant frequency supported by the silver metasurface gate pad. **b**, Measured reflection spectra of fabricated optical modulators under transverse-magnetic (TM) polarized (red) and transverse-electric (TE) polarized (blue) normal illumination. Solid and semi-transparent curves represent the reflection spectra for the devices with and without WS_2 monolayers, respectively. The grey curve indicates the reflection spectrum of the flat silver gate pad. **c**, Mechanism of the enhanced intensity modulation of the reflected beam. A one-port, two-coupled cavity system is used to describe the essential physics of the optical modulator. The total decay rate of the excitons in WS_2 can be tuned via electrical gating. **d**, Fitted (dashed red) and simulated (grey) reflection spectra of the designed optical modulator. The calculated reflection spectra with different decay rates of the excitons in WS_2 are also shown in different coloured dashed curves. The inset shows the calculated reflectance at the exciton resonant wavelength as a function of the decay rate of excitons. **e**, Optical image (taken from the top gate pad side) of the fabricated optical modulator array. Scale bar, 500 μm. **f**, Optical image (taken from the substrate side) of one fabricated optical modulator in the array. Scale bar, 50 μm. **g**, Polarization-resolved photoluminescence map of the fabricated optical modulator.

compared with the modulation using a suspended WS_2 monolayer (~0.5% modulation; Supplementary Fig. 3).

Enhancing the radiative decay of excitons with a metasurface

The nanopatterned metal surface can improve the modulator's performance by enhancing both the excitation field and radiative decay for the excitons in the WS_2 monolayer via the Purcell effect. Purcell demonstrated that the radiative decay rate of emitters can be increased by placing them in an optical cavity[36]. To understand the increased modulation for our structure in more detail, it is important to realize that the grooves patterned in our gate pad facilitate the excitation of several optical resonances capable of concentrating the in-plane electric fields within the WS_2 monolayer. First, normally incident light can excite guided resonances for surface plasmon polaritons (SPPs) on the periodically nanopatterned metal surface. This possibility emerges as the periodic perturbation can fold the dispersion curve of the SPPs into the first Brillouin zone (Fig. 2a)[37]. We choose a 305 nm period to couple the incident 615 nm light. By doing so, two optical modes (one bright, one dark) can be found at the Γ-point near the exciton resonance frequency. Figure 2b shows the measured reflection spectra of a fabricated modulator with the patterned gate pad. The efficient excitation of the bright optical mode from the lower photonic band produces a large reflection dip around 620 nm. A second, small dip is also observed in the reflection spectrum around 565 nm, corresponding to the symmetry-protected dark mode (that is, a bound state in the continuum) from the upper photonic band (Supplementary Fig. 4).

As SPPs are longitudinal electron-density waves, they can only be excited under transverse magnetic polarized illumination, where the electric field is normal to the length of the grooves. Meanwhile, the exciton resonance can be probed in the reflection spectrum under transverse electric polarized illumination (Supplementary Fig. 5), where it is not overpowered by the SPP modes. It is clear that the exciton resonance is spectrally well-aligned with the bright optical mode supported by the nanopatterned gate pad. Upon excitation of the combined system, the WS_2 monolayer can resonantly absorb and then coherently re-emit the light back into the coupled SPP mode with a notably increased excitation and radiative decay rate for the excitons due to the concentrated vacuum field as well as the boosted local density of optical states. At the same time, the periodically patterned gate pad can ultimately decouple the excited SPPs from the surface back into free space. At this point it is important to note that the period of the perturbation on the metal gate pad is sufficiently small that emitted and decoupled light cannot decay into diffracted orders. As such, it is appropriate to term the patterned gate pad a metasurface. For the metasurface, strong interference effects are expected between the radiating SPPs that are coupled to the WS_2 monolayer and the non-resonant background produced by a direct reflection from the metal surface. Active manipulation of this interference can be leveraged to achieve dynamic reflection modulation.

Figure 2c graphically illustrates how the intensity of the reflected beam can be modified via carrier injection into the WS_2 monolayer through the optical coupling between the coherently excited excitons and the above-analysed bright quasi-guided SPP mode supported by the metasurface. In the absence of the optical coupling, the total decay rate of excitons for a neutralized sample ($\hbar\gamma_{x0}$) is ~28.9 meV, extracted from the simulations based on the optical constants measured via ellipsometry (Supplementary Fig. 6). These very large decay rates are quite typical for TMDCs at room temperature and come with substantially broadened exciton resonances that are incapable of achieving efficient modulation[26]. The resonances broaden even further with

electrical gating (V) as additionally injected electrons notably shorten the exciton lifetime[38]. Despite the broadening, our metasurface gate pad can help achieve good modulation. To understand this, we first develop an optical rate-equation model to quantitatively link the reduction in the exciton lifetime to the applied electrical bias (Supplementary Note 1). We then explain the optical behaviour of our device under transverse-magnetic-polarized illumination by developing a temporal coupled mode theory (CMT)[39] for two-coupled cavities with one port (Supplementary Note 2). The metasurface serves as one of these cavities and the resonant excitonic system serves as the second cavity. As the full-wave simulations, the CMT assumes a linear, coherent response for our materials. We find that the predicted reflection spectrum modulation obtained from CMT is consistent with our wave-optics simulations (Figs. 1e and 2d). By fitting the CMT to the simulation data, we can extract key modelling parameters that capture the behaviour of our system. We find that we can ignore the direct radiative decay channel of excitons into free space ($\hbar\gamma_{xr} \approx 2.3$ meV) as their optical coupling to the SPP mode ($\hbar g_{cavx} \approx 17.7$ meV) is found to be around eight-times faster (Supplementary Fig. 6). The optical properties of the metasurface cavity can be designed at will and are described by its resonant wavelength ($2\pi c/\omega_{cav} \approx 615$ nm), radiative decay rate ($\hbar\gamma_{cavr} \approx 14.4$ meV) and non-radiative decay rate ($\hbar\gamma_{cava} \approx 4.9$ meV) for the chosen metasurface geometry used in the simulation (Fig. 1e,f). The exciton resonant frequency (ω_x) is also to some degree tunable through band gap engineering[40]. The CMT produces the following expression for the gate-dependent reflectance of the modulator:

$$R(\omega, V) \cong \left| -1 + \frac{2\gamma_{cavr}}{i(\omega - \omega_{cav}) + \gamma_{cavr} + \gamma_{cava} + \frac{(g_{cavx})^2}{i(\omega-\omega_x)+\gamma_x(V)}} \right|^2. \quad (1)$$

The importance of the electrically tunable term $(g_{cavx})^2/(i(\omega - \omega_x) + \gamma_x(V))$ is determined by the strength of the direct coupling between the metasurface cavity mode and exciton resonance g_{cavx} as well as the exciton resonance frequency ω_x and bias-dependent exciton decay rate $\gamma_x(V)$. This term captures the ability of the SPPs to store energy in the exciton resonance and retrieve it. To see how this term can boost the modulation efficiency, it is of value to explore the case in which the metasurface cavity is on resonance ($\omega = \omega_{cav}$). Here, the expression for the reflectance can be simplified to:

$$R(V) \cong \left| -1 + \frac{2\eta_{cav}}{1 + \frac{\Gamma}{i\delta_x + \gamma_x(V)}} \right|^2, \quad (2)$$

where $\eta_{cav} = \gamma_{cavr}/(\gamma_{cavr} + \gamma_{cava})$ determines the scattering efficiency of the metasurface cavity, and $\delta_x = \omega_{cav} - \omega_x$ is the detuning for the coupled system; $\Gamma = g_{cavx}{}^2/(\gamma_{cavr} + \gamma_{cava})$ quantifies the Purcell-enhanced excitation and radiative decay rate of excitons from and back into the quasi-guided SPP mode of the metasurface cavity. The calculated time evolution of the coupled system confirms the accelerated decay process for the excitons via the Purcell effect (Supplementary Fig. 7). When the excitons are switched off ($\gamma_x \approx \infty$), the reflectance is simply determined by the scattering efficiency of the metasurface cavity $R_{max} = |2\eta_{cav} - 1|^2$, and the near-unity reflection can be achieved if the metasurface is lossless. To maximize the modulation ratio, we need to operate the modulator near the critical coupling point ($R_{min} = 0$) when the exciton is switched on, leading to the relation $2\eta_{cav} - 1 = \frac{\Gamma}{i\delta_x + \gamma_{x0}}$. It is thus clear that the enhanced coupling of the quasi-guided SPP mode with the excitons in the WS_2 monolayer enables the achievement of critical coupling. We highlight that the modulation $\left(\Delta R \approx \left|\frac{\Gamma}{i\delta_x + \gamma_{x0}}\right|^2\right)$ can be efficient only if the Purcell-enhanced radiative decay rate ($\hbar\Gamma \approx 16.2$ meV) becomes comparable with the sum rate of other unwanted decay processes (~$\hbar\gamma_{x0} \approx 28.9$ meV), and the exciton resonance is degenerate with the quasi-guided SPP mode ($\delta_x \approx 0$). At this point, it is worth noting that the enhanced radiative decay rate provided by the metasurface would also be beneficial if some of the excitonic broadening at room temperatures had been due to dephasing processes. Although this project is focused on maximizing the modulator performance, it is interesting to note that other valuable operating regimes, such as strong coupling, can be achieved in the same configuration as well (Supplementary Fig. 8).

Efficient intensity modulation of free-space light beams

To further demonstrate our platform and design concept, we fabricate optical modulators starting from a millimetre-scale single crystal monolayer WS_2 flake exfoliated from bulk crystal[41] onto a sapphire substrate (Supplementary Fig. 9). This allows us to pattern a device array consisting of 150 optical modulators on a 1 cm^2 chip using standard cleanroom processing (Fig. 2e). An optical image (taken from the substrate side) of one fabricated optical modulator in the array highlights the details of the configuration (Fig. 2f). A 50 × 50 μm^2 isolated WS_2 monolayer pad is electrically connected to a U-shaped gold electrode, and a 30-μm-sized silver metasurface gate pad is fabricated in the centre, spaced by a 15-nm-thick Al_2O_3 film that serves as the gate insulator. The measured polarization-resolved photoluminescence map (Fig. 2g; see also Supplementary Fig. 10 for detailed photoluminescence spectra in the maps) confirms the exciton–plasmon performance of the silver metasurface gate pad, where the exciton emission is enhanced by a factor of ~2 for the transverse-magnetic polarization that supports SPPs (see Supplementary Fig. 11 for simulations of the Purcell-enhanced photoluminescence).

We note that the resonant wavelength of the SPP mode can be tuned systematically by gradually changing the periodicity of the perturbation (Fig. 3a). This is particularly important for maximizing the modulation effect, as the optical mode supported by the silver metasurface pad needs to be degenerate with the exciton resonance. For a fabricated modulator with the optimal periodicity, we measure the changes in the reflection spectrum from a 10 × 10 μm^2 device area using a fibre-coupled confocal microscope as a function of the gating voltage, which was applied from −3 V to 3 V in 3 V steps (Fig. 3b). We also need to apply hole injection here to bring the WS_2 monolayer as closely back to its neutral state as possible, as exfoliated TMDC monolayers are usually found to be n-doped due to chalcogen vacancies as well as extrinsic doping from charges on the substrate and electron-beam exposure (Supplementary Fig. 12)[42,43]. We find that the modulator operates very close to the critical coupling condition when the WS_2 monolayer is neutralized at −3 V, and gradually deviates from it by electron doping. A 3 dB modulation ratio (at 627 nm), as well as a 10% reflectance change (at 621 nm), are experimentally demonstrated as shown in Fig. 3c. This absolute reflectance change is 20-times larger than our previous ionic-liquid gating experiment in the absence of the optical coupling[17], and is quite comparable to a recent low-temperature solid-state back-gating experiment at 4 K with hexagonal boron nitride encapsulation[27]. All of these features are in good agreement with the simulated results shown in Fig. 1e,f, except that the modulation is weaker in the experiment. We attribute this to the weaker exciton resonance oscillator strength in the WS_2 monolayer caused by the additional defect generation[44] and inhomogeneous broadening due to the dielectric and charge disorder in the atomic layer deposition (ALD)-deposited Al_2O_3 encapsulation (Supplementary Fig. 13). Furthermore, the insubstantial carrier injection limited by a very thin, non-uniform gate insulator restricts the exciton lifetime modulation range[45] (Supplementary Note 3).

We also perform photoluminescence spectrum modulation (Supplementary Fig. 14) and lifetime modulation (Supplementary Fig. 15) measurements to study the exciton dynamics and to verify the role

https://doi.org/10.1038/s41566-023-01250-9

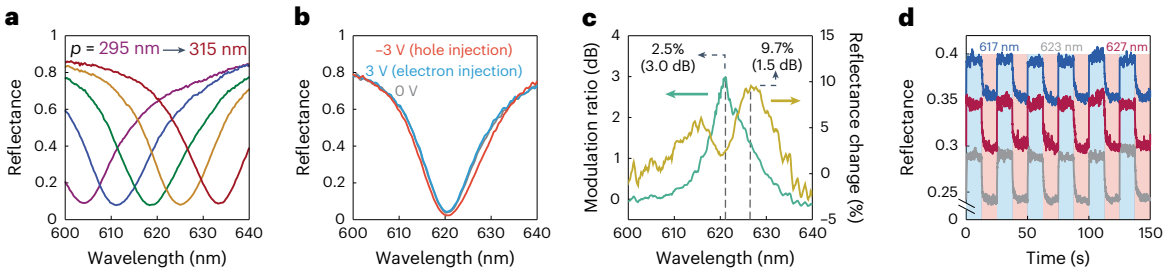

Fig. 3 | Intensity modulation of the reflected beam via electrical gating. **a**, Measured reflection spectra of a series of fabricated optical modulators with the perturbation periodicity changing from 295 nm (purple) to 315 nm (maroon) in 5 nm steps. **b**, Measured reflection spectrum modulation of a fabricated optical modulator in the device array (p = 305 nm). The gating voltage is applied from −3 V (hole injection, red) to 3 V (electron injection, blue) in 3 V steps. This optical modulator has the optimal perturbation periodicity to spectrally match the quasi-guided SPP mode with the exciton resonance almost perfectly. **c**, Extracted modulation ratio (green) and absolute reflectance change (yellow) spectra from the measurements in **b**. A 3 dB modulation ratio and a 10% reflectance change are observed in the experiment. **d**, Measured alternating current modulation of the reflected beam from the fabricated optical modulator. Different coloured curves indicate focused supercontinuum laser illumination with different centre wavelengths. The shadings represent the gating voltage applied, cycled between 3 V (blue) and −3 V (red). All of the spectra in **a**–**d** are collected under transverse-magnetic-polarized normal illumination.

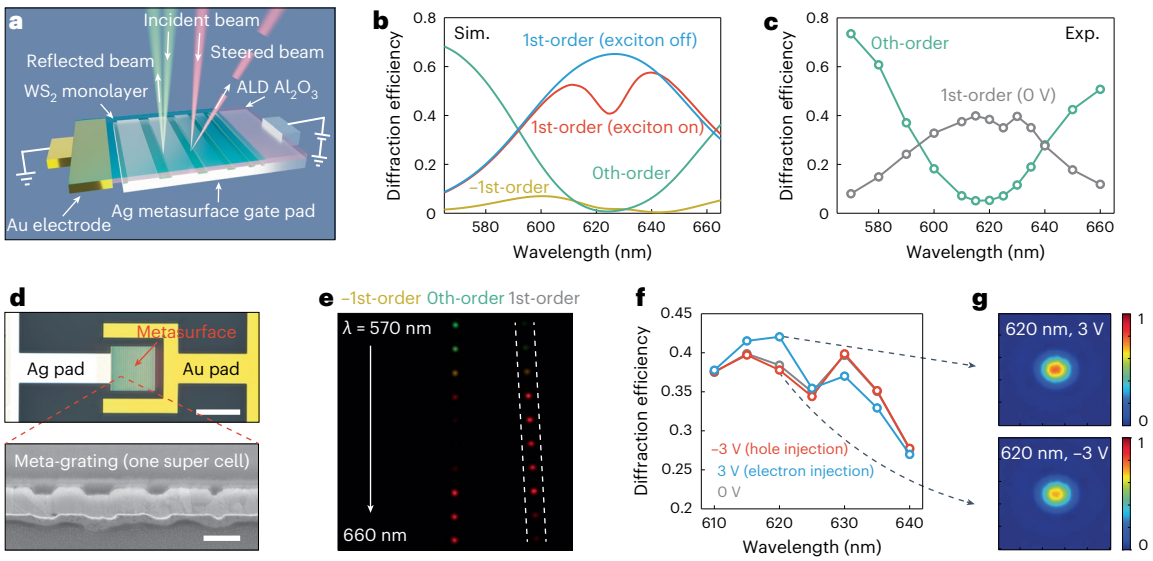

Fig. 4 | Monolayer WS_2 light-field modulators with a beam-steering function. **a**, Schematic of a monolayer WS_2 light-field modulator with a beam-steering function. The periodic perturbation is replaced by super cells that can provide a 2π phase gradient across one cell. **b**,**c**, Simulated (**b**) and measured (**c**) diffraction efficiency spectra of the light-field modulator under transverse-magnetic-polarized normal illumination. The first-order diffraction is maximized around the exciton resonance wavelength, whereas the zeroth- and negative-first-order diffraction are suppressed. **d**, Optical (top) and cross-sectional SEM (bottom) images of the fabricated light-field modulator. Scale bars, 30 μm (top); 200 nm (bottom). **e**, Optical images of the back-focal plane of the fabricated light-field modulator. The incident wavelength is tuned from 570 nm to 660 nm in steps of 10 nm. **f**, Measured intensity modulation of the first-order diffracted beam via electrical gating. The gating voltage is applied from −3 V (hole injection, orange) to 3 V (electron injection, blue) in 3 V steps. The incident wavelength is tuned from 610 nm to 640 nm in 5 nm steps. **g**, Optical images of the modulated first-order diffracted beam with an incident wavelength of 620 nm.

of carrier injection in the optical modulation[38,42,46]. An alternating current modulation experiment is further conducted by measuring the real-time reflected beam intensity with a focused narrow-band illumination (NA = 0.2, FWHM ≈ 5 nm), as shown in Fig. 3d. We find that the focused beam spectrally averages the modulation effect, as a quasi-constant (~5%) reflectance modulation is achieved in a ~15 nm bandwidth (Supplementary Fig. 16), revealing the possibility to modulate beams in a certain bandwidth as well. We also confirm the good reversibility of the fabricated optical modulator. The observed modulation speed is mainly limited by the large resistor-capacitor time constant of the circuit for electrical gating due to the substantial contact and access resistance between the gold electrode and the modulated WS_2 monolayer (Supplementary Fig. 17), which can be improved by proper contact engineering and device configuration optimization[44,47]. We note that in principle a gigahertz-speed modulation in such a solid-state gating device is possible and has been reported in similar configurations[48].

Achieving dynamic control over light fields

Finally, we extend the concept from the reflection modulation to a more general dynamic control over light fields. As a proof of concept, we demonstrate a monolayer WS_2 light-field modulator with a beam-steering function, where a silver metasurface with a constant phase gradient serves as the gate pad, and the intensity of the first-order diffracted beam is electrically modulated (Fig. 4a). In principle, the 2π full-phase control needed for a gradient metasurface can be achieved in the over-coupling regime by varying the filling fraction of the grooves (Supplementary Fig. 18)[49]. We subsequently conduct a global optimization to take into account the coupling between neighbouring grooves due to the propagating SPPs. Figure 4b shows the simulated diffraction

efficiency spectra of the optimized monolayer WS_2 light-field modulator. It is designed so that the first-order diffraction dominates the zeroth-order specular beam near the exciton resonant wavelength. The redirected beam can efficiently be modulated by controlling the intensity of the exciton resonance of the WS_2 monolayer. We again systematically pattern a light-field modulator array on a 1 cm^2 fused silica chip as shown in Fig. 4d. The measured diffraction efficiency spectra of a fabricated light-field modulator match the simulated results very well (Fig. 4c). The efficient beam steering is also visualized by a series of optical images of the modulator that are taken in the Fourier plane with the incident wavelength range adjusted from 570 nm to 660 nm in 10 nm steps (Fig. 4e). We conduct the modulation experiment by measuring the intensity change of the first-order diffracted beam via electrical gating as a function of the incident wavelength (Fig. 4f). A clear modulation is observed near the exciton resonant wavelength, reaching its maximum at 620 nm with a ~5% change in its diffraction efficiency (0.5 dB modulation ratio). The observed asymmetric lineshape in the modulation may result from the trion resonance which is not considered in the simulations[42]. Such a modulation can be easily recognized from the optical images of the first-order diffracted beam with different gating voltages (Fig. 4g).

Discussion

Altogether, these results demonstrate a novel free-space optical modulator platform that leverages the highly tunable optical properties of a semiconductor monolayer and an optimized photonic environment to boost the exciton–light interaction to achieve effective modulation at room temperature. This platform can lead to various practical applications that require fast modulation of free-space optical signals. At a higher level, this work shows the notable benefits of radiative decay engineering for excitons in 2D semiconductors in the performance of optical modulation that complements significant efforts in improving materials quality.

Online content

Any methods, additional references, Nature Portfolio reporting summaries, source data, extended data, supplementary information, acknowledgements, peer review information; details of author contributions and competing interests; and statements of data and code availability are available at https://doi.org/10.1038/s41566-023-01250-9.

References

1. Mak, K. F., Lee, C., Hone, J., Shan, J. & Heinz, T. F. Atomically thin MoS_2: a new direct-gap semiconductor. *Phys. Rev. Lett.* **105**, 136805 (2010).
2. Splendiani, A. et al. Emerging photoluminescence in monolayer MoS_2. *Nano Lett.* **10**, 1271–1275 (2010).
3. Lien, D.-H. et al. Electrical suppression of all nonradiative recombination pathways in monolayer semiconductors. *Science* **364**, 468–471 (2019).
4. Radisavljevic, B. & Kis, A. Mobility engineering and a metal–insulator transition in monolayer MoS_2. *Nat. Mater.* **12**, 815–820 (2013).
5. Das, S. et al. Transistors based on two-dimensional materials for future integrated circuits. *Nat. Electron.* **4**, 786–799 (2021).
6. Wu, S. et al. Monolayer semiconductor nanocavity lasers with ultralow thresholds. *Nature* **520**, 69–72 (2015).
7. Ye, Y. et al. Monolayer excitonic laser. *Nat. Photon.* **9**, 733–737 (2015).
8. Wilson, N. P., Yao, W., Shan, J. & Xu, X. Excitons and emergent quantum phenomena in stacked 2D semiconductors. *Nature* **599**, 383–392 (2021).
9. Chernikov, A. et al. Electrical tuning of exciton binding energies in monolayer WS_2. *Phys. Rev. Lett.* **115**, 126802 (2015).
10. Jauregui, L. A. et al. Electrical control of interlayer exciton dynamics in atomically thin heterostructures. *Science* **366**, 870–875 (2019).
11. Raja, A. et al. Coulomb engineering of the bandgap and excitons in two-dimensional materials. *Nat. Commun.* **8**, 15251 (2017).
12. Castellanos-Gomez, A. et al. Local strain engineering in atomically thin MoS_2. *Nano Lett.* **13**, 5361–5366 (2013).
13. Li, Y. et al. Measurement of the optical dielectric function of monolayer transition-metal dichalcogenides: MoS_2, $MoSe_2$, WS_2, and WSe_2. *Phys. Rev. B* **90**, 205422 (2014).
14. Chernikov, A. et al. Exciton binding energy and nonhydrogenic Rydberg series in monolayer WS_2. *Phys. Rev. Lett.* **113**, 076802 (2014).
15. Yu, Y. et al. Giant gating tunability of optical refractive index in transition metal dichalcogenide monolayers. *Nano Lett.* **17**, 3613–3618 (2017).
16. Datta, I. et al. Low-loss composite photonic platform based on 2D semiconductor monolayers. *Nat. Photon.* **14**, 256–262 (2020).
17. van de Groep, J. et al. Exciton resonance tuning of an atomically thin lens. *Nat. Photon.* **14**, 426–430 (2020).
18. Biswas, S., Grajower, M. Y., Watanabe, K., Taniguchi, T. & Atwater, H. A. Broadband electro-optic polarization conversion with atomically thin black phosphorus. *Science* **374**, 448–453 (2021).
19. Willner, A. E. et al. Optical communications using orbital angular momentum beams. *Adv. Opt. Photon.* **7**, 66–106 (2015).
20. Schwarz, B. Mapping the world in 3D. *Nat. Photon.* **4**, 429–430 (2010).
21. Silva, A. et al. Performing mathematical operations with metamaterials. *Science* **343**, 160–163 (2014).
22. Lin, X. et al. All-optical machine learning using diffractive deep neural networks. *Science* **361**, 1004–1008 (2018).
23. Liu, M. et al. A graphene-based broadband optical modulator. *Nature* **474**, 64–67 (2011).
24. Xu, Q., Schmidt, B., Pradhan, S. & Lipson, M. Micrometre-scale silicon electro-optic modulator. *Nature* **435**, 325–327 (2005).
25. Back, P., Zeytinoglu, S., Ijaz, A., Kroner, M. & Imamoğlu, A. Realization of an electrically tunable narrow-bandwidth atomically thin mirror using monolayer $MoSe_2$. *Phys. Rev. Lett.* **120**, 037401 (2018).
26. Scuri, G. et al. Large excitonic reflectivity of monolayer $MoSe_2$ encapsulated in hexagonal boron nitride. *Phys. Rev. Lett.* **120**, 037402 (2018).
27. Li, M., Biswas, S., Hail, C. U. & Atwater, H. A. Refractive index modulation in monolayer molybdenum diselenide. *Nano Lett.* **21**, 7602–7608 (2021).
28. Epstein, I. et al. Near-unity light absorption in a monolayer WS_2 Van der Waals heterostructure cavity. *Nano Lett.* **20**, 3545–3552 (2020).
29. Selig, M. et al. Excitonic linewidth and coherence lifetime in monolayer transition metal dichalcogenides. *Nat. Commun.* **7**, 13279 (2016).
30. Sönnichsen, C. et al. Drastic reduction of plasmon damping in gold nanorods. *Phys. Rev. Lett.* **88**, 077402 (2002).
31. Dahmen, C., Schmidt, B. & von Plessen, G. Radiation damping in metal nanoparticle pairs. *Nano Lett.* **7**, 318–322 (2007).
32. Lamprecht, B. et al. Metal nanoparticle gratings: influence of dipolar particle interaction on the plasmon resonance. *Phys. Rev. Lett.* **84**, 4721–4724 (2000).
33. Bogdanov, S. I., Boltasseva, A. & Shalaev, V. M. Overcoming quantum decoherence with plasmonics. *Science* **364**, 532–533 (2019).
34. Grange, T. et al. Reducing phonon-induced decoherence in solid-state single-photon sources with cavity quantum electrodynamics. *Phys. Rev. Lett.* **118**, 253602 (2017).

35. Horng, J. et al. Engineering radiative coupling of excitons in 2D semiconductors. *Optica* **6**, 1443–1448 (2019).
36. Purcell, E. M. Spontaneous emission probabliities at radio frequencies. *Phys. Rev.* **69**, 681 (1946).
37. Hooper, I. R. & Sambles, J. R. Dispersion of surface plasmon polaritons on short-pitch metal gratings. *Phys. Rev. B* **65**, 1–9 (2002).
38. Chen, P. et al. Approaching the intrinsic exciton physics limit in two-dimensional semiconductor diodes. *Nature* **599**, 404–410 (2021).
39. Fan, S., Suh, W. & Joannopoulos, J. D. Temporal coupled-mode theory for the Fano resonance in optical resonators. *J. Opt. Soc. Am. A* **20**, 569 (2003).
40. Chaves, A. et al. Bandgap engineering of two-dimensional semiconductor materials. *npj 2D Mater. Appl.* **4**, 29 (2020).
41. Liu, F. et al. Disassembling 2D van der Waals crystals into macroscopic monolayers and reassembling into artificial lattices. *Science* **367**, 903–906 (2020).
42. Mak, K. F. et al. Tightly bound trions in monolayer MoS_2. *Nat. Mater.* **12**, 207–211 (2013).
43. Daus, A. et al. High-performance flexible nanoscale transistors based on transition metal dichalcogenides. *Nat. Electron.* **4**, 495–501 (2021).
44. McClellan, C. J., Yalon, E., Smithe, K. K. H., Suryavanshi, S. V. & Pop, E. High current density in monolayer MoS_2 doped by AlO_x. *ACS Nano* **15**, 1587–1596 (2021).
45. McDonnell, S. et al. HfO_2 on MoS_2 by atomic layer deposition: adsorption mechanisms and thickness scalability. *ACS Nano* **7**, 10354–10361 (2013).
46. Morozov, S., Wolff, C. & Mortensen, N. A. Room-temperature low-voltage control of excitonic emission in transition metal dichalcogenide monolayers. *Adv. Opt. Mater.* **9**, 2101305 (2021).
47. Allain, A., Kang, J., Banerjee, K. & Kis, A. Electrical contacts to two-dimensional semiconductors. *Nat. Mater.* **14**, 1195–1205 (2015).
48. Andersen, T. I. et al. Beam steering at the nanosecond time scale with an atomically thin reflector. *Nat. Commun.* **13**, 3431 (2022).
49. Park, J., Kang, J.-H., Kim, S. J., Liu, X. & Brongersma, M. L. Dynamic reflection phase and polarization control in metasurfaces. *Nano Lett.* **17**, 407–413 (2017).

Methods

Numerical simulations

We perform 2D finite-element simulations in the frequency domain using the commercial software package COMSOL (COMSOL, Inc.) to study the optical properties of the designed monolayer WS_2 free-space optical modulator. We apply periodic boundary conditions to simulate the properties of the modulator with periodic perturbations. The same boundary condition is also applied to the entire super cell for the light-field modulator. The modulator is illuminated by a normally incident plane wave and all the possible diffraction orders are added as ports in the simulation. The Purcell enhancement is calculated by placing a linear electric dipole in the WS_2 monolayer plane and calculating the ratio between the power emitted from the dipole in the modulator configuration and in the vacuum. Perfectly matched layers are added at the boundaries to converge the simulation.

The WS_2 monolayer is modelled as a 0.618-nm-thick dielectric slab[13] with an in-plane refractive index determined by ellipsometry measurements on a commercially available (2D Semiconductors) chemical-vapour-deposition-grown WS_2 monolayer on a sapphire substrate[50]. The exciton resonance contribution is separated from the dielectric background of the monolayer WS_2 by fitting the dielectric constant from an ellipsometry measurement with two Lorentz oscillators for the A and B excitons and a Tauc–Lorentz oscillator for the inter-band transitions. The out-of-plane refractive index of WS_2 monolayer is artificially set as 1. The dispersion of silver is described in a Drude model with a constant dielectric background from the inter-band transitions, in which the plasma frequency and damping constant in the Drude model are fitted to match the observed SPP dispersion. The refractive index of Al_2O_3 by ALD and SiO_2 by electron-beam evaporation is set as 1.67 and 1.48, both determined by ellipsometry measurements. The refractive index of sapphire and fused silica substrate is set as 1.77 and 1.46, respectively.

Device fabrication

Millimetre-scale single crystal WS_2 monolayer exfoliation. WS_2 monolayers are exfoliated from bulk WS_2 crystals (HQ graphene) onto a sapphire or fused silica substrate using gold tape exfoliation[41]. For preparation of the gold tape, a 100-nm-thick gold layer is deposited onto a clean silicon wafer (Nova wafers) with an electron-beam evaporator (Kurt J. Lesker). The Au/Si is subsequently spin coated with a layer of polyvinylpyrrolidone (PVP, Fischer) as a sacrificial layer for protection against contamination. A piece of thermal release tape (3196 S, Semiconductor Corp) is pressed onto the PVP/Au layer to peel off the gold surface from the silicon substrate, revealing a clean and flat gold surface templated by the flat silicon wafer. The templated-stripped gold surface is pressed upon a cleaved WS_2 crystal surface to peel a monolayer off the bulk crystal. The thermal release tape/PVP/Au/WS_2 layer is later pressed onto the substrate. After releasing the tape by heating on a hotplate at 95 °C and dissolving the PVP layer in deionized water, the remaining gold is etched away in a homemade KI/I_2 etchant solution, leaving monolayers on the substrate. The remaining etchant and solvent are rinsed with water and isopropyl alcohol, and dried with a N_2 gun.

Nanofabrication of monolayer WS_2 free-space optical modulators. (1) Gold electrode and marker patterning. We start the fabrication from a millimetre-scale WS_2 monolayer on a 1 cm^2 sapphire substrate. A 500-nm-thick MMA/180-nm-thick polymethyl methacrylate (PMMA) double-layer is spin coated onto the WS_2 monolayer to serve as a positive-tone electron-beam resist layer. A thin conductive polymer layer (E-Spacer 300Z) is then spin coated to mitigate charging effects during the electron-beam lithography process (JEOL 6300 100 kV system, electron-beam current = 9 nA, dose = 500 μC cm^{-2}). The development is performed in a methyl isobutyl ketone:isopropyl alcohol (1:1) solution for 45 s; 100-nm-thick gold is then deposited by electron-beam evaporation (Kurt J. Lesker), followed by overnight lift-off in acetone. (2) WS_2 monolayer pad isolation. The PMMA/MMA double-layer electron-beam lithography, as described in (1), is conducted again to define the shape of the WS_2 monolayer pad to be isolated. We use a larger electron-beam current (30 nA) to save the writing time for large features. Low-energy (30 W) argon sputtering (Oxford PlasmaPro 80) is conducted to only etch the WS_2 monolayer away, and the remaining resist is removed by rinsing the sample in acetone overnight. (3) Gate oxide deposition. A 1-nm-thick aluminium film is first deposited on the substrate by electron-beam evaporation (AJA) and then oxidized overnight into Al_2O_3 (~2 nm thick) as the seeding layer. A 13-nm-thick Al_2O_3 dielectric layer is then deposited via atomic layer deposition at 200 °C (Cambridge Nanotech Fiji or a home-built tool[43]). (4) SiO_2 nano-strip patterning. The PMMA/MMA double-layer electron-beam lithography, as described in (1), is conducted again to define the shape of the SiO_2 nano-strip array. To improve the writing resolution for fine structures, a thinner MMA layer (100 nm) is spin coated and we apply a smaller electron-beam current (0.5 nA) during the exposure. A 17-nm-thick SiO_2 layer is then deposited by electron-beam evaporation (AJA), followed by an overnight lift-off in acetone. (5) Silver top gate pad patterning. The PMMA/MMA double-layer electron-beam lithography, as described in (1), is conducted again to define the shape of the silver top gate pad. 180-nm-thick silver is then deposited by electron-beam evaporation (Kurt J. Lesker), followed by a 20-nm-thick platinum deposition in the same tool to protect silver from oxidization. The entire fabrication process is graphically illustrated in Supplementary Fig. 9.

Nanofabrication of monolayer WS_2 light-field modulators. The fabrication process of the monolayer WS_2 light-field modulator is similar to that of the optical modulator described above. The difference is that, first, we start the fabrication from a millimetre-scale WS_2 monolayer exfoliated on a 1 cm^2 fused silica substrate, and second, 40-nm-thick SiO_2 are deposited in making SiO_2 nano-strips to achieve a larger radiative decay rate for the quasi-guided SPP mode supported by the metasurface gate pad, so that the modulator is operated in the over-coupling regime.

Integration with printed circuit boards for modulation experiment. To test the optical response of the fabricated modulators with electrical gating, we wire bond the gold electrodes as well as the sillver top gate pads to a home-made printed circuit board (PCB) (Supplementary Fig. 19). A hole is drilled on the PCB to allow the reflection measurement with illumination through the substrate.

Optical measurements

Direct current electrical gating. The fabricated optical modulator is electrically gated by a source meter (Keithley 2612), while the gold electrode (WS_2 monolayer) is grounded. The leakage current is monitored when we apply the electrical bias. The maximum gating voltage that we can safely add onto the 15-nm-thick gate oxide was found to be ±3 V, which corresponds to a critical electric field of ~0.2 V nm^{-1}. This number is smaller than the reported breakdown electric field in thick Al_2O_3 (~1 V nm^{-1}). We attribute this to the non-uniformity of the ALD Al_2O_3 deposited on the WS_2 monolayer, as well as the enhanced local electric field due to the sharp edges of the silver metasurface gate pad.

Bright-field reflection measurements. We perform the optical reflection measurement using a Nikon C2 confocal microscope. Unpolarized white light from a halogen lamp is used for top-illumination of the sample through a ×4 objective (Olympus, NA = 0.1). The reflection signal is then collected by the same objective and analysed by a linear polarizer. A confocal scanner with a 40 μm pinhole is used to spatially select the reflection signal (collection area diameter ~10 μm) which is analysed using a SpectraPro 2300i spectrometer and Pixis Si CCD (−70 °C detector temperature). When we conduct the serious measurement on the

modulator with the optimized periodicity, to fully take advantage of the spectral resolution of the spectrometer, the slit width is set as 5 µm, and a blazed grating (λ_B = 500 nm) with a groove density of 300 lines per millimetre is selected. The aperture stop is fully closed to collimate the top illumination as well as possible. The reported spectra are averaged by five frames (160 s integration time each). Meanwhile, a larger slit width (25 µm) and a grating with less groove density (150 lines per millimetre) are used to select the modulator with the optimal periodicity in the device array (Fig. 3a) for faster signal collection (40 s integration time each). All of the reflection spectra are normalized by the reflection spectrum of a protected silver mirror (Thorlabs, PF10-03-P01). The reflection from the top surface of the substrate has been removed through post-data processing, and the spectra shown in the figures have been smoothed using MATLAB.

Spectrally and spatially resolved photoluminescence measurements. We conduct the spectrally and spatially resolved photoluminescence measurement of the WS_2 monolayer in the optical modulator using a Witec confocal Raman imaging microscope. A 532 nm laser is fibre-coupled to the microscope and is tightly focused by a ×50 objective (Nikon, NA = 0.55) to optically pump the WS_2 monolayer. The photoluminescence emission is collected by the same objective, filtered by a dichroic filter cube as well as a long-pass filter (Semrock, LP03-532RU-25), and polarized by a linear polarizer if necessary. A 100-µm-diameter fibre is used as the confocal pinhole and is coupled to a spectrometer to analyse the spectral properties of the photoluminescence emission. The sample (attached on the PCB) is placed on a motorized stage to spatially map the photoluminescence emission with submicrometre resolution.

Time-resolved photoluminescence measurements. We conduct the time-resolved photoluminescence measurement of the WS_2 monolayer in the optical modulator using a second Witec confocal Raman imaging microscope. The photoluminescence excitation and collection process is similar to what is described above, but with a 485 nm paused laser (PicoQuant P-C-485, repetition frequency = 40 MHz) and a different ×50 objective (Zeiss, NA = 0.55). A 100-µm-diameter fibre is used as the confocal pinhole and is coupled to an avalanche photodiode (APD; Micro Photon Devices) to measure the lifetime of excitons by time-correlated single-photon counting.

Reflection measurements with alternating current modulation. We perform the optical reflection measurement with alternating current electrical modulation using the second Witec confocal Raman imaging microscope as described above. A supercontinuum laser and an acousto-optic tunable filter (Fianium) are used to generate and tune the wavelength of the laser beam (~5 nm bandwidth). The laser is fibre-coupled to the microscope and focused on the sample by a ×10 objective (Zeiss, NA = 0.2). The reflection signal is then collected by the same objective and detected in real time by the fibre-coupled APD. The square wave alternating current voltage (±3 V) applied to the optical modulator is generated by a function generator (Agilent). The measured reflectance of the optical modulator is normalized by the reflection from the flat silver pad next to the optical modulator.

Diffraction efficiency modulation measurements. We perform the diffraction efficiency measurement of the light-field modulator using the same Nikon C2 confocal microscope as described above. A supercontinuum laser and acousto-optic tunable filter (NKT superK) are used to generate and tune the wavelength of the laser beam (~5 nm bandwidth). The laser is fibre-coupled to the microscope and illuminated on the sample by a ×50 objective (Nikon, NA = 0.6). The field stop in the laser illumination path is fully closed, only leaving a 20-µm-diameter hexagonal pinhole in the field of view for signal collection. The diffracted lights from the light-field modulator are then collected by the same objective and the optical image of the Fourier plane of the light-field modulator is captured by a complementary metal–oxide–semiconductor camera (Thorlabs) with the inserted Bertrand lens. The diffraction efficiency of the light-field modulator is then extracted from the intensity integral of the diffracted spots in the optical images taken at the Fourier plane and is normalized by the reflection from the flat silver pad next to the optical modulator.

Data availability

All key data that support the findings of this study are included in the article and its Supplementary Information. Further datasets and raw measurements are available from the corresponding author on reasonable request.

References

50. van de Groep, J., Li, Q., Song, J.-H., Kik, P. G. & Brongersma, M. L. Impact of substrates and quantum effects on exciton line shapes of 2D semiconductors at room temperature. *Nanophotonics* https://doi.org/10.1515/nanoph-2023-0193 (2023).

Acknowledgements

We would like to acknowledge funding from an AFOSR MURI grant (grant no. FA9550-17-1-0002) and the US Department of Energy (grant no. DE-FG07-ER46426).

Author contributions

Q.L. and M.L.B. conceived the research idea. Q.L. built the model, performed the design and fabrication of optical modulators with input from J.v.d.G. Q.L., J.-H.S. and F.X. performed the experimental characterization of the optical modulators. A.C.J. and F.L. prepared monolayer WS_2 samples. J.H. performed wire-bonding for electrical characterization. A.D. and E.P. helped with atomic layer deposition. Y.J.L. helped with photoluminescence measurement. M.L.B. supervised the project. All of the authors contributed to writing the manuscript.

Competing interests

The authors declare no competing interests.

Additional information

Supplementary information The online version contains supplementary material available at https://doi.org/10.1038/s41566-023-01250-9.

Correspondence and requests for materials should be addressed to Mark L. Brongersma.

Peer review information *Nature Photonics* thanks Alex Krasnok and Zongfu Yu for their contribution to the peer review of this work.

nature photonics

Article

https://doi.org/10.1038/s41566-023-01250-9

A Purcell-enabled monolayer semiconductor free-space optical modulator

In the format provided by the authors and unedited

This PDF file includes:

Supplementary Notes 1-3
Supplementary Figs. 1 to 19

Supplementary Note 1. Modelling the exciton lifetime with an optical rate equation.

We analytically illustrate the relation between the lifetime of the excitons and the gating voltage applied to the optical modulator with an optical rate-equation model [1] as discussed below. We only consider the exciton and trion generation here by assuming that the illumination power is low. An optical rate equation to describe the optical absorption at a steady state induced by the exciton resonance is as follows:

$$G = n_{\mathrm{X}}\left(\gamma_{\mathrm{Xr}} + \gamma_{\mathrm{Xph}} + \gamma_{\mathrm{Xe}} + \gamma_{\mathrm{EX}}\right), \quad (1)$$

$$G_{\mathrm{T}} = n_{\mathrm{X}}\gamma_{\mathrm{EX}} = n_{\mathrm{T}}\gamma_{\mathrm{T}}. \quad (2)$$

G is the generation rate of free electron-hole pairs by illumination, and n_{X} and n_{T} refer to the density of excitons and trions. G_{T} is the generation rate of trions. γ_{EX} denotes the exchange rate of excitons to form trions by combining an additional electron, and γ_{T} is the total decay rate of trions, which is assumed as a constant here to simplify the discussion. γ_{Xr}, γ_{Xph}, and γ_{Xe} correspond to the radiative, phonon-assisted non-radiative, and electron-assisted non-radiative decay rate of excitons. We ignore the hole-assisted scattering here since we focus on an electron-doped system. The phonon-assisted non-radiative decay rate can be estimated from the sum of all the phonon modes that can scatter excitons into a different state [2]. It is expected that when additional electrons are injected into the monolayer semiconductor, the Coulomb interaction between the electron-hole pairs is screened, and therefore the binding energy of excitons is decreased. Consequently, more phonon modes become available to scatter or directly dissociate electron-hole pairs. Given the fact that the electron doping level is low in the solid-state gating configuration (~10^{12}/cm^2), we can apply the Taylor expansion to the phonon-assisted non-radiative decay around the charge neutrality point:

$$\gamma_{\mathrm{Xph}} = \gamma_{\mathrm{Xph0}} + A_{\mathrm{ph1}}n_{\mathrm{e}} + A_{\mathrm{ph2}}{n_{\mathrm{e}}}^2 + \cdots \quad (3)$$

γ_{Xph0} is the phonon-assisted non-radiative decay at the charge neutrality state, and A_{ph1} and A_{ph2} are expansion coefficients. On the other hand, the electron-assisted non-radiative decay rate can be modeled as:

$$\gamma_{\mathrm{Xe}} = A_{\mathrm{e}}n_{\mathrm{e}}. \quad (4)$$

A_{e} represent the capture probabilities for exciton-electron interactions, and n_{e} is the free electron density. The density of excitons and trions can be linked together via a law of mass action:

$$n_{\mathrm{T}} = Tn_{\mathrm{X}}n_{\mathrm{e}}. \quad (5)$$

T denotes the trion formation coefficient. γ_{T} Charge conservation further links the density of trions and electrons to the electron doping level:

$$N = N_{\mathrm{in}} + N_{\mathrm{ex}} = n_{\mathrm{e}} + n_{\mathrm{T}}. \quad (6)$$

N represents the total electron doping density, being the sum of the intrinsic doping N_{in} (defects, charges from substrates) and extrinsic doping $N_{\mathrm{ex}} = c_{ox}V/q$ via electrical gating, where c_{ox} is the oxide capacitance, V is the gating voltage, and q is the electron charge. By combining all these equations together, Eq. (1) can be re-written as:

$$G = n_{\mathrm{X}}\left(\gamma_{\mathrm{X_r}} + \gamma_{\mathrm{Xph0}} + \left(A_{\mathrm{ph1}} + A_{\mathrm{e}} + \gamma_{\mathrm{T}}T\right)\frac{N_{\mathrm{in}} + \frac{c_{\mathrm{ox}}V}{q}}{1 + Tn_{\mathrm{X}}} + A_{\mathrm{ph2}}\left(\frac{N_{\mathrm{in}} + \frac{c_{\mathrm{ox}}V}{q}}{1 + Tn_{\mathrm{X}}}\right)^2\right). \quad (7)$$

When the density of excitons is low ($n_{\mathrm{ex}} \ll n_{\mathrm{e}}$), the above equation can be further simplified as:

$$G \cong n_{\mathrm{X}}(A + BV + CV^2), \quad (8)$$

where

$$A = \gamma_{\mathrm{Xr}} + \gamma_{\mathrm{Xph0}} + \left(A_{\mathrm{ph1}} + A_{\mathrm{e}} + \gamma_{\mathrm{T}}T\right)N_{\mathrm{in}} + A_{\mathrm{ph2}}{N_{\mathrm{in}}}^2, \quad (9)$$

$$B = \left(A_{\mathrm{ph1}} + A_{\mathrm{e}} + \gamma_{\mathrm{T}}T + 2A_{\mathrm{ph2}}N_{\mathrm{in}}\right)\frac{c_{ox}}{q}, \quad (10)$$

$$C = A_{\mathrm{ph2}}\left(\frac{c_{ox}}{q}\right)^2. \quad (11)$$

Equation 8 clearly shows that $A + BV + CV^2$ is the total decay rate of excitons, which can be tuned efficiently via electrical gating as illustrated in Fig. 3c and Supplementary Fig. 12. At the charge neutrality point $N_{\mathrm{in}} + \frac{c_{ox}V}{q} = 0$, the total decay rate of excitons goes back to $\gamma_{\mathrm{Xr}} + \gamma_{\mathrm{Xph0}}$ as expected.

Supplementary Note 2. Detailed temporal coupled mode theory for optical coupling between the exciton resonance and the metasurface in the optical modulator.

To better understand the optical coupling between the exciton resonance and the metasurface in the designed optical modulator, and especially how the reflection modulation can benefit from such an optical coupling, we model the modulator as an optical system consisting of two coupled cavities with one port, and apply a temporal coupled mode theory (CMT) for analysis [3]. The metasurface serves as one of these cavities and facilitates the coupling to free-space photons. It both allows for the resonant optical excitation of quasi-guided surface plasmon polariton (SPP) waves and controls their decoupling back into free space radiation. The resonant excitonic system serves as the second cavity. It can be coherently excited by the SPPs and the excitons can in turn couple back into the metasurface cavity through the coherent re-excitation of SPPs. This coupled dynamics is captured by the following equations:

$$\frac{d}{dt}\begin{pmatrix} a_{\mathrm{cav}} \\ a_{\mathrm{x}} \end{pmatrix} = \begin{pmatrix} \mathrm{i}\omega_{\mathrm{cav}} - \gamma_{\mathrm{cavr}} - \gamma_{\mathrm{cava}} & \mathrm{i}g_{\mathrm{cavx}} - \gamma_0 \\ \mathrm{i}g_{\mathrm{cavx}} - \gamma_0 & \mathrm{i}\omega_{\mathrm{x}} - \gamma_{\mathrm{xr}} - \gamma_{\mathrm{xa}} \end{pmatrix}\begin{pmatrix} a_{\mathrm{cav}} \\ a_{\mathrm{x}} \end{pmatrix} + \begin{pmatrix} \kappa_{\mathrm{cav}} \\ \kappa_{\mathrm{x}} \end{pmatrix} {S_1}^+, \tag{12}$$

where, $a_{\mathrm{cav(x)}}$, $\omega_{\mathrm{cav(x)}}$, $\gamma_{\mathrm{cavr(xr)}}$, $\gamma_{\mathrm{cava(xa)}}$ represent the normalized amplitude, resonant frequency, radiative decay rate, as well as non-radiative decay rate for the optical resonance supported by the metasurface cavity and the exciton resonance, respectively. ${S_1}^+ = e^{i\omega t}$ is the incident plane wave acting as the input of the port, and $\kappa_{\mathrm{cav(x)}}$ is the incoupling constant from the free-space plane wave to the cavity. g_{cavx} represents the direct coupling between the two cavities, and γ_0 quantifies the super- (sub-) radiance when the two cavities emit photons into the same port. The output from the port ${S_1}^-$ is dictated by the scattering matrix:

$${S_1}^- = -{S_1}^+ + d_{\mathrm{cav}} a_{\mathrm{cav}} + d_{\mathrm{x}} a_{\mathrm{x}}, \tag{13}$$

where $d_{\mathrm{cav(x)}}$ represents the outcoupling constant from the cavity to the free-space plane wave. The energy conservation sets up the relation between the outcoupling constant and the radiative decay rates of the cavities:

$$|d_i|^2 = 2\gamma_{\mathrm{ir}}, \qquad {d_{\mathrm{x}}}^* d_{\mathrm{cav}} = 2\gamma_0, \qquad i = \mathrm{x}, \mathrm{cav}. \tag{14}$$

Time reversal symmetry further dictates that the incoupling and outcoupling constant have to satisfy the following relations:

$$\kappa_i = d_i, \qquad {d_i}^* = d_i, \quad i = \mathrm{x}, \mathrm{cav}. \tag{15}$$

After some algebra, we can get:

$$\kappa_i = d_i = \sqrt{2\gamma_{\mathrm{ir}}}, \qquad i = \mathrm{x}, \mathrm{cav}. \tag{16}$$

$$\gamma_0 = \sqrt{\gamma_{\mathrm{cavr}}\gamma_{\mathrm{xr}}}. \tag{17}$$

(1). Steady-state analysis.

By plugging all these relations into the dynamic coupled equations, at the steady state we find:

$$r = \frac{{S_1}^-}{{S_1}^+}$$
$$= -1 + \frac{\frac{\mathrm{i}(g_{\mathrm{cavx}} + \mathrm{i}\sqrt{\gamma_{\mathrm{cavr}}\gamma_{\mathrm{xr}}})2\sqrt{\gamma_{\mathrm{cavr}}\gamma_{\mathrm{xr}}}}{\mathrm{i}(\omega - \omega_{\mathrm{x}}) + \gamma_{\mathrm{xr}} + \gamma_{\mathrm{xa}}} + 2\gamma_{\mathrm{cavr}}}{\mathrm{i}(\omega - \omega_{\mathrm{cav}}) + \gamma_{\mathrm{cavr}} + \gamma_{\mathrm{ava}} + \frac{(g_{\mathrm{cavx}} + \mathrm{i}\sqrt{\gamma_{\mathrm{cavr}}\gamma_{\mathrm{xr}}})^2}{\mathrm{i}(\omega - \omega_{\mathrm{x}}) + \gamma_{\mathrm{xr}} + \gamma_{\mathrm{xa}}}}$$
$$+ \frac{\frac{\mathrm{i}(g_{\mathrm{cavx}} + \mathrm{i}\sqrt{\gamma_{\mathrm{cavr}}\gamma_{\mathrm{xr}}})2\sqrt{\gamma_{\mathrm{cavr}}\gamma_{\mathrm{xr}}}}{\mathrm{i}(\omega - \omega_{\mathrm{cav}}) + \gamma_{\mathrm{cavr}} + \gamma_{\mathrm{cava}}} + 2\gamma_{\mathrm{xr}}}{\mathrm{i}(\omega - \omega_{\mathrm{x}}) + \gamma_{\mathrm{xr}} + \gamma_{\mathrm{xa}} + \frac{(g_{\mathrm{cavx}} + \mathrm{i}\sqrt{\gamma_{\mathrm{cavr}}\gamma_{\mathrm{xr}}})^2}{\mathrm{i}(\omega - \omega_{\mathrm{cav}}) + \gamma_{\mathrm{cavr}} + \gamma_{\mathrm{cava}}}}. \quad (18)$$

The first term in the above equation comes from the reflection from the non-resonant background, while the second and third term corresponds to the light scattering from the metasurface cavity and the excitons, respectively. Given the fact that at room temperature the radiative decay rate of excitons is one order of magnitude smaller than its non-radiative decay rate, the direct coupling strength to the cavity, as well as the decay rate of the metasurface cavity, we may ignore this minor contribution by assuming $\gamma_{\mathrm{xr}} \cong 0$, and therefore we can greatly simplify the above equation as follows:

$$r \cong -1 + \frac{2\gamma_{\mathrm{cavr}}}{\mathrm{i}(\omega - \omega_{\mathrm{cav}}) + \gamma_{\mathrm{cavr}} + \gamma_{\mathrm{cava}} + \frac{(g_{\mathrm{cavx}})^2}{\mathrm{i}(\omega - \omega_{\mathrm{x}}) + \gamma_{\mathrm{x}}(V)}}. \quad (19)$$

We note that $\gamma_{\mathrm{x}}(V)$ represents the total decay rate of excitons in the absence of the optical coupling, which can be tuned via electrical gating V, increasing from $\gamma_{\mathrm{x0}} = \gamma_{\mathrm{xr}} + \gamma_{\mathrm{xa0}}$ at the neutrality point toward infinitely large by additional electron injection. Such a simplified equation gives us a very clear understanding of the role of the tunable exciton resonance in determining the reflection from the designed optical modulator. In the presence of the efficient coupling between the exciton resonance and the metasurface cavity, the exciton excitation effectively becomes an additional tunable non-radiative decay channel of the metasurface cavity $\frac{(g_{\mathrm{cavx}})^2}{\mathrm{i}(\omega - \omega_{\mathrm{x}}) + \gamma_{\mathrm{x}}(V)}$. When the metasurface cavity is on resonance ($\omega = \omega_{\mathrm{cav}}$), the reflection coefficient of the modulator can be further written as:

$$r \cong -1 + \frac{2\eta_{\mathrm{cav}}}{1 + \frac{\Gamma}{\mathrm{i}\delta_{\mathrm{x}} + \gamma_{\mathrm{x}}(V)}}. \quad (20)$$

Here, the term $\eta_{\mathrm{cav}} = \gamma_{\mathrm{cavr}}/(\gamma_{\mathrm{cavr}} + \gamma_{\mathrm{cava}})$ determines the scattering efficiency of the metasurface cavity, and $\Gamma = {g_{\mathrm{cavx}}}^2/(\gamma_{\mathrm{cavr}} + \gamma_{\mathrm{cava}})$ denotes the Purcell-enhanced radiative decay rate of excitons into the metasurface cavity. $\delta_{\mathrm{x}} = \omega_{\mathrm{cav}} - \omega_{\mathrm{x}}$ is the detuning for the coupled

system. When the exciton resonance is turned off ($\gamma_{\mathrm{x}} \sim \infty$), the reflection coefficient of the modulator is simply determined by the scattering efficiency of the metasurface cavity $r_{\max} = 2\eta_{\mathrm{cav}} - 1$, and the near-unity reflection can be achieved if the metasurface cavity is lossless. To maximize the modulation ratio, we need to operate the modulator near the critical coupling point ($r_{\min} = 0$) at the cavity resonant wavelength when the exciton is turned on, leading to the relation $2\eta_{\mathrm{cav}} - 1 = \frac{\Gamma}{\mathrm{i}\delta_{\mathrm{x}} + \gamma_{\mathrm{x0}}}$. It is thus clear that the modulation ($\Delta r = r_{\max} - r_{\min} \sim \frac{\Gamma}{\mathrm{i}\delta_{\mathrm{x}} + \gamma_{\mathrm{x0}}}$) can be efficient only if the Purcell-enhanced radiative decay rate (Γ) becomes comparable to the sum rate of other unwanted decay processes of excitons ($\sim \gamma_{\mathrm{x0}}$), and the exciton resonance degenerates with the metasurface cavity mode ($\delta_{\mathrm{x}} \sim 0$).

We further fit the simulated results with the CMT model to extract the related parameters ($\hbar\gamma_{\mathrm{xr}}$ = 2.3 meV, $\hbar\gamma_{\mathrm{xa0}}$ = 26.6 meV, $\hbar\gamma_{\mathrm{cavr}}$ = 14.4 meV, $\hbar\gamma_{\mathrm{cava}}$ = 4.9 meV, $\hbar g_{\mathrm{cavx}}$ = 17.7 meV) and confirm the validity of the theory as shown in Fig. 2d and Supplementary Fig. 6. During the fitting process, the reflection from the non-resonant background is also treated as a variable r_{b} to take the optical loss from the Ag mirror into account.

We also note that the dephasing of excitons in the WS_2 monolayer should, in principle, also play a role in determining the reflection from the designed optical modulator. The impact of dephasing is not captured by the presented model (beyond possible contributions to the broadening of the exciton linewidth as measured by ellipsometry). A quantum-mechanical model needs to be developed to describe the difference between the self-interference of the exciton emission and its interference with the background reflection in a limited coherence time [4,5]. It is worth noting that both the CMT and full-field simulations describe the same physics and do not fully capture the impact of dephasing processes.

(2). Eigen-mode analysis.

To study the intrinsic properties of the coupled system, we can temporarily turn off the out-coupling channel. Therefore, the dynamic equation can be rewritten as below:

$$\frac{d}{dt}\begin{pmatrix} a_{\mathrm{cav}} \\ a_{\mathrm{x}} \end{pmatrix} = \begin{pmatrix} \mathrm{i}\tilde{\omega}_{\mathrm{cav}} & \mathrm{i}\tilde{g}_{\mathrm{cavx}} \\ \mathrm{i}\tilde{g}_{\mathrm{cavx}} & \mathrm{i}\tilde{\omega}_{\mathrm{x}} \end{pmatrix}\begin{pmatrix} a_{\mathrm{cav}} \\ a_{\mathrm{x}} \end{pmatrix}. \tag{21}$$

In the presence of the efficient coupling between the metasurface cavity and the exciton resonance, two hybridized modes $|\pm\rangle$ occur to replace the unperturbed metasurface cavity mode $|\mathrm{cav}\rangle$ and the exciton mode $|\mathrm{x}\rangle$ as the eigenmodes through the diagonalization of the Hamiltonian of the coupled system. The dynamic equation of the coupled system is then written under the new basis:

$$\frac{d}{dt}\begin{pmatrix} a_{+} \\ a_{-} \end{pmatrix} = \begin{pmatrix} \mathrm{i}\tilde{\omega}_{+} & 0 \\ 0 & \mathrm{i}\tilde{\omega}_{-} \end{pmatrix}\begin{pmatrix} a_{+} \\ a_{-} \end{pmatrix}, \tag{22}$$

where:

$$\mathrm{i}\tilde{\omega}_{\pm} = \mathrm{i}\omega_{\pm} - \gamma_{\pm} = \frac{\mathrm{i}(\tilde{\omega}_{\mathrm{cav}} + \tilde{\omega}_{\mathrm{x}}) \pm \mathrm{i}\sqrt{(\tilde{\omega}_{\mathrm{cav}} + \tilde{\omega}_{\mathrm{x}})^2 - 4\left(\tilde{\omega}_{\mathrm{cav}}\tilde{\omega}_{\mathrm{x}} - \tilde{g}_{\mathrm{cavx}}{}^2\right)}}{2}. \quad (23)$$

$a_{\pm}$ represent the normalized amplitude of the hybridized eigenmodes. The relation between the new basis and the unperturbed basis is given below:

$$|+\rangle = A|\mathrm{cav}\rangle + B|\mathrm{x}\rangle, \quad |-\rangle = C|\mathrm{cav}\rangle + D|\mathrm{x}\rangle, \quad (24)$$

where:

$$A(C) = \frac{\tilde{g}_{\mathrm{cavx}}}{\sqrt{|\tilde{g}_{\mathrm{cavx}}|^2 + \left|\tilde{\omega}_{\pm} - \tilde{\omega}_{\mathrm{cav}}\right|^2}}, \quad B(D) = \frac{\tilde{\omega}_{\pm} - \tilde{\omega}_{\mathrm{cav}}}{\sqrt{|\tilde{g}_{\mathrm{cavx}}|^2 + \left|\tilde{\omega}_{\pm} - \tilde{\omega}_{\mathrm{cav}}\right|^2}}. \quad (25)$$

Therefore, given the initial state of the coupled system to be $|\varphi_0\rangle = a_{\mathrm{cav0}}|\mathrm{cav}\rangle + a_{\mathrm{x0}}|\mathrm{x}\rangle = a_{+0}|+\rangle + a_{-0}|-\rangle$, the time evolution of the coupled system can be expressed as:

$$\begin{aligned} |\varphi(t)\rangle &= a_{+0}e^{\mathrm{i}\tilde{\omega}_{+}t}|+\rangle + a_{-0}e^{\mathrm{i}\tilde{\omega}_{-}t}|-\rangle \\ &= \left(a_{+0}Ae^{\mathrm{i}\tilde{\omega}_{+}t} + a_{-0}Ce^{\mathrm{i}\tilde{\omega}_{-}t}\right)|\mathrm{cav}\rangle \\ &+ \left(a_{+0}Be^{\mathrm{i}\tilde{\omega}_{+}t} + a_{-0}De^{\mathrm{i}\tilde{\omega}_{-}t}\right)|\mathrm{x}\rangle. \end{aligned} \quad (26)$$

We can now switch back to the unperturbed basis to look at the energy hopping between the metasurface cavity mode and the excitons:

$$|a_{\mathrm{cav}}(t)|^2 = \left|a_{+0}Ae^{\mathrm{i}\tilde{\omega}_{+}t} + a_{-0}Ce^{\mathrm{i}\tilde{\omega}_{-}t}\right|^2, \quad |a_{\mathrm{x}}(t)|^2 = \left|a_{+0}Be^{\mathrm{i}\tilde{\omega}_{+}t} + a_{-0}De^{\mathrm{i}\tilde{\omega}_{-}t}\right|^2. \quad (27)$$

Specifically, we can set up the initial state as $|\varphi_0\rangle = |\mathrm{x}\rangle$ to check the decay process of the excitons. By plugging all the extracted parameters from the reflection simulation (Supplementary Fig. 6), the time-resolved exciton decay process for the coupled system is shown in Supplementary Fig. 7. In the presence of the metasurface cavity, the exciton decay rate is accelerated noticeably, indicating that the enhanced radiative decay rate becomes comparable to the rate of other unwanted non-radiative decay and dephasing processes that dominate the population decay in the vacuum. We note that the designed modulator operates in an intermediate regime between the typical weak coupling and strong coupling regime, revealed by the gentle wiggles in the calculated time evolution of the exciton decay process.

(3). Realizing strong coupling in the proposed optical modulator configuration.

Although the designed optical modulator shown in the main text (Figs. 1e, f) operates in the weak coupling regime, we note that the strong coupling can be realized in such a configuration as well. Such a strong coupling occurs uniformly across the entire two-dimensional plane and can be probed directly from the reflection measurement. This is in shape contrast to most of the reported

strong coupling between the excitons and the plasmonic nano-antennas, where only excitons in a very small area in proximity to the nano-antenna can efficiently interact with the nano-antenna, and the mode splitting is only visible in the scattering spectrum via the dark-field measurement.

In order to achieve the strong coupling based on the proposed modulator design, the coupling strength needs to be enhanced by placing the WS_2 monolayer closer to the metasurface gate pad. Additionally, the radiative decay rate of the metasurface cavity can be suppressed by narrowing the width of the groove perturbation on the metasurface gate pad. For example, by reducing the gate oxide thickness from 15 nm to 1 nm (i.e., few-layer hBN) and narrowing the groove width from 78 nm to 5 nm, mode splitting occurs naturally in the simulated reflection spectrum (Supplementary Fig. 8a). The corresponding decay rates can be extracted based on the CMT model ($\hbar\gamma_{\mathrm{cavr}}$ ~ 3.8 meV, $\hbar\gamma_{\mathrm{cava}}$ ~ 4.0 meV, $\hbar g_{\mathrm{cavx}}$ ~ 22.8 meV), and the calculated time evolution of the coupled system visualizes a weak Rabi oscillation resulting from the nature of strong coupling (Supplementary Fig. 8b).

The Rabi oscillation can be further enhanced by reducing the non-radiative decay rate of the excitons, which can be realized by cooling down the sample to cryogenic temperatures. For instance, if we don't change any rates extracted from the design in Supplementary Fig. 8a but set up the non-radiative decay rate of the excitons ($\hbar\gamma_{\mathrm{xa0}}$) as 5 meV, the Rabi oscillation is found to be enhanced significantly from the calculated time evolution of the coupled system (Supplementary Fig. 8c).

Supplementary Note 3. Discussions on further improving the performance of the demonstrated optical modulator.

Although a 10 percentage-point reflection change and a 3 dB modulation ratio are successfully observed in the experiment (Fig. 3 b, c), we admit that there is still a clear gap (~ 4 times) between the performance of the fabricated devices and the ideal ones in the simulations. We attribute this to the weaker exciton resonance in the WS_2 monolayer caused by the additional doping and the inhomogeneous broadening due to the dielectric and charge disorder from ALD Al_2O_3 encapsulation (Supplementary Fig. 13) as compared with a prime sample. In addition, the insubstantial carrier injection limited by a very thin, non-uniform gate insulator restricts the exciton lifetime modulation range. In our experiment, we apply a 3V gating voltage on a 15 nm-thick gate oxide, corresponding to a vertical DC electric field of ~ 0.20 V/nm. This field strength is in the same order as the previously reported result (65 V on a 280 nm-thick SiO_2 gate oxide, corresponding to ~ 0.23 V/nm [6]), but still far away from the breakdown voltage of good-quality ALD Al_2O_3 (~ 1V/nm). However, we do suffer from the relatively low-quality, non-uniform ALD oxide deposited on the WS_2 monolayer, which restricts the applied voltage to 3V in our experiment.

Both challenges mentioned above are linked to the choice of a proper insulating material that can passivate the 2D semiconductors uniformly and hold large enough electric fields to allow more carriers injected into the 2D semiconductors. Hexagonal boron nitride (hBN) is considered as the best candidate so far thanks to its atomically flat nature and wide band gap, and it has been commonly used these days for encapsulation in fundamental 2D semiconductor studies. We envision that, by replacing the ALD Al_2O_3 layer with a multi-layer hBN in the modulator design, the modulation effect in the experiment will be enhanced further and can approach the performance of ideal devices shown in the simulations. Nevertheless, the major limitation of hBN encapsulation is that the hBN layer prepared by mechanical exfoliation can only provide a tens-of-micrometer-sized encapsulation area each time, and precise alignment is required during the transfer process. Therefore, even if we may be able to fabricate a few devices from this method (which should be good enough for fundamental studies), we cannot extend this concept to chip- or wafer-scale manufacture.

We want to emphasize that, in the design of practical optoelectronic devices, the scalability for mass production is as much important as the optimal performance of a single device that we can achieve. Given the fact that many high-performance devices based on 2D semiconductors have been reported, scalability has become the major challenge to prevent us from commercializing 2D semiconductor-based devices. From this point of view, we sincerely believe that the successful demonstration of a 2D semiconductor-based optical modulator array using all standard cleanroom processing is very meaningful to the community. For this reason, although it has been proved in our experiment that the ALD Al_2O_3 may not be the best choice for maximizing the device performance, it seems to be the only mature standard cleanroom processing that allows us to pattern modulators in the chip scale at this moment.

We are optimistic about improving the device performance while maintaining scalability in mass production in the future. Chemical vapor deposition and molecular beam epitaxy have been proved to be able to grow reasonably high-quality 2D semiconductors [7,8] and hBN layers [9,10] in the wafer scale, and the comprehensive 2D layer transfer system is also developed recently [11,12]. There is no doubt that all these emerging technologies will greatly facilitate the mass production of electronic and optoelectronic devices based on 2D semiconductors in a systematic way.

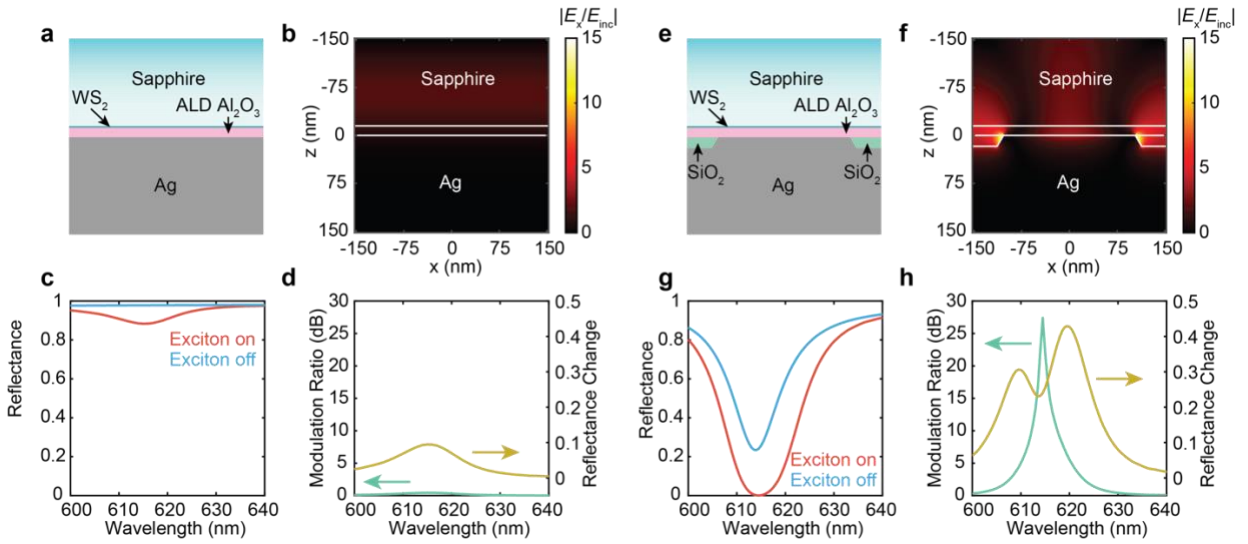

Supplementary Fig. 1 | Optical modulation with a conventional flat Ag gate pad. a, Detailed cross-sectional geometry and **b,** the corresponding electric-field distribution of the conventional optical modulator with a flat Ag gate pad under the normally incident plane-wave illumination. The incident wavelength is 615 nm. **c,** Simulated reflection spectra of the conventional optical modulator under plane-wave illumination. The exciton resonance in WS_2 is switched on (orange) and off (blue) artificially by first separating the exciton resonance contribution from the dielectric background in the dielectric function of the WS_2 monolayer and then keeping (on-state) or removing (off-state) this contribution in the dielectric function. **d,** Extracted modulation ratio (green) and absolute reflectance change (yellow) from the simulations in **c**. **e-h,** Copied from Figs. 1c-f in the main text for a direct comparison.

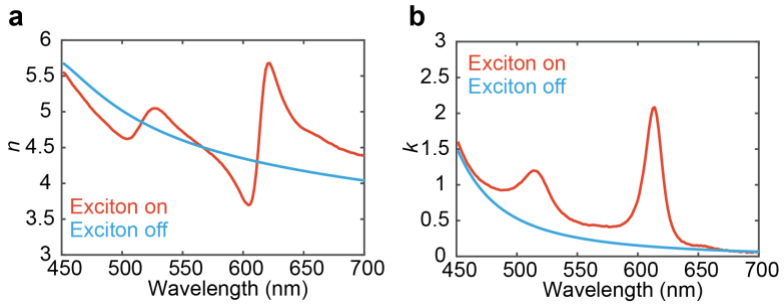

Supplementary Fig. 2 | Refractive-index change of a WS_2 monolayer when the exciton resonance is switched on and off artificially. a, Real and **b,** imaginary part of the refractive index of a WS_2 monolayer when the exciton resonance is switched on (neutral state) and off (electron-doped state). The refractive index used for the 'exciton on' status is determined by ellipsometry measurements on a commercially available (2D Semiconductors) chemical-vapor-deposition (CVD) grown WS_2 monolayer on a sapphire substrate. We assume that this sample is close to the charge neutrality point, and therefore the exciton resonance is not damped. The dielectric background of the WS_2 monolayer, which is used to calculate the dielectric constant for the 'exciton off' status, is then separated from the exciton resonance contribution by fitting the dielectric constant from the ellipsometry measurement with two Lorentz oscillators for the A and B excitons and a Tauc-Lorentz oscillator for the inter-band transitions as the background.

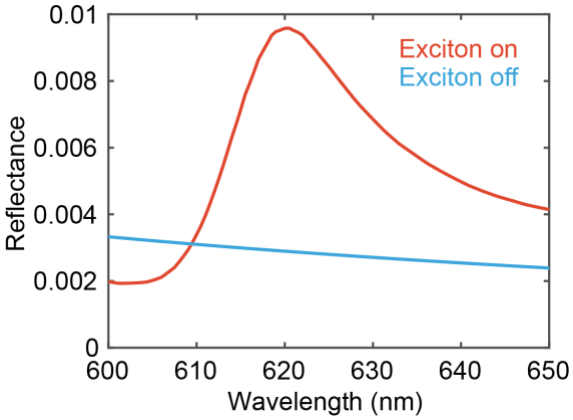

Supplementary Fig. 3 | Reflection modulation with a suspended WS_2 monolayer. The figure shows the simulated reflection spectra of a suspended WS_2 monolayer when the exciton resonance is switched on and off artificially. Only a ~0.6 percentage-point reflection change is observed, originating from the limited light scattering from the exciton resonance due to the much smaller intrinsic radiative decay rate of excitons compared with its non-radiative decay and dephasing rate.

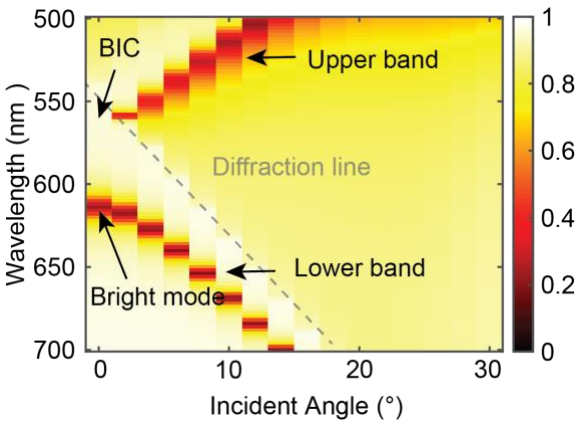

Supplementary Fig. 4 | Optical modes supported by the Ag metasurface gate pad. The figure shows the simulated reflection spectra of the designed optical modulator as a function of the incident angle under TM-polarized illumination. We find two photonic bands in the wavelength range we study here. These photonic bands originate from the dispersion relation of the surface plasma polaritons at the Ag/dielectric interface. At Γ point, the mode from the lower band can be excited efficiently by the free-space light, leading to a clear dip in the reflection spectrum. Meanwhile, the mode from the upper band disappears at Γ point. This results from the fact that this mode has an anti-symmetric electric-field distribution in each period, and therefore cannot be excited by the normally incident plane wave for the symmetry reason. Such a mode is also commonly referred to as symmetry-protected bound states in the continuum (BIC).

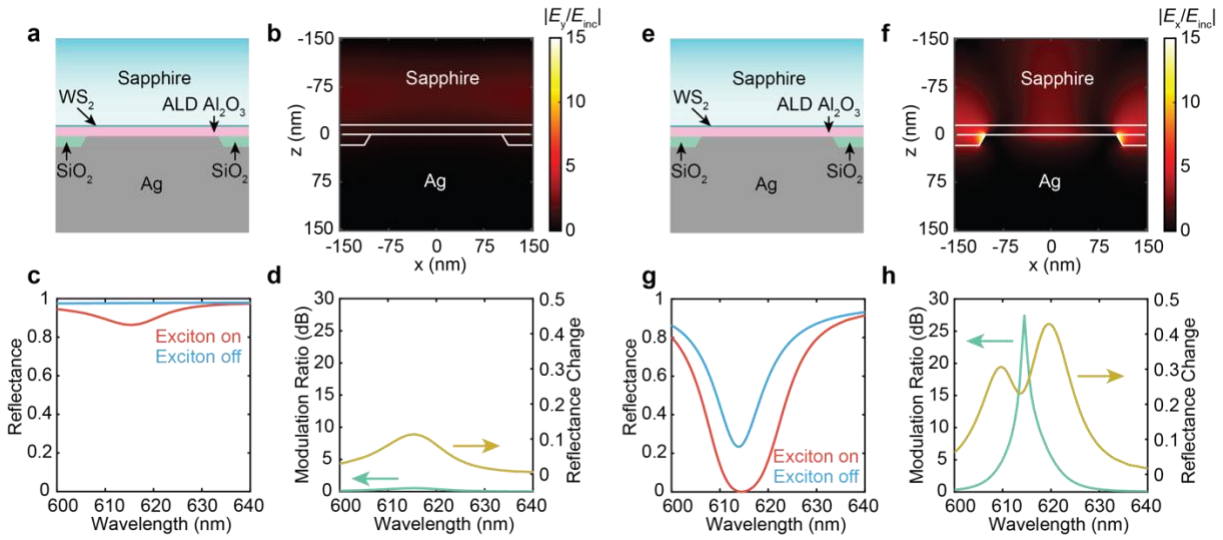

Supplementary Fig. 5 | Optical modulation with a metasurface Ag gate pad under TE-polarized illumination. a, Detailed cross-sectional geometry and **b,** the corresponding in-plane electric-field distribution of the designed optical modulator under TE-polarized plane-wave illumination. The incident wavelength is 615 nm. **c,** Simulated reflection spectra of the designed optical modulator under TE-polarized plane-wave illumination. The exciton resonance in WS_2 is turned on (orange) and off (blue) artificially by first separating the exciton resonance contribution from the dielectric background in the dielectric function of the WS_2 monolayer and then keeping (on-state) or removing (off-state) this contribution in the dielectric function. **d,** Extracted modulation ratio (green) and absolute reflectance change (yellow) from the simulations in **c**. **e-h,** Copied from Figs. 1c-f in the main text for a direct comparison with the TM-polarized illumination.

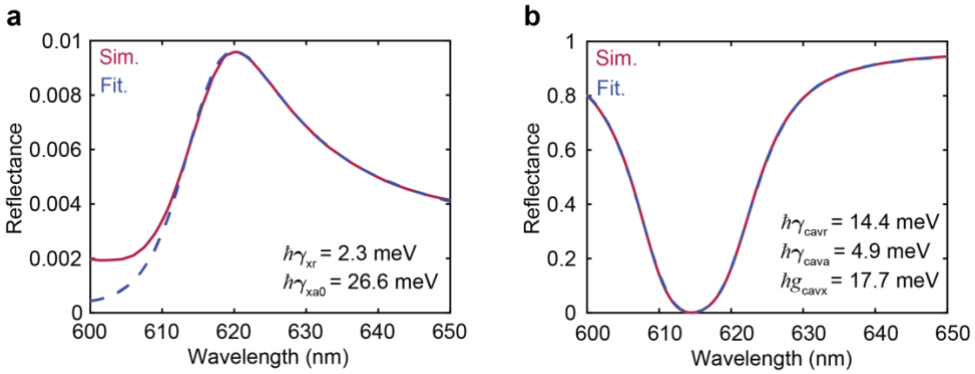

Supplementary Fig. 6 | Extracting the decay rates of excitons into different channels by fitting the temporal coupled mode theory model with the full-field simulation results. a, Simulated and fitted reflection spectrum of a suspended WS_2 monolayer and **b,** the designed optical modulator. From the curve fitting, we find that the non-radiative decay rate of excitons ($\hbar\gamma_{\mathrm{xa0}}$ ~ 26.6 meV) is one order of magnitude larger than its radiative decay rate ($\hbar\gamma_{\mathrm{xr}}$ ~ 2.3 meV). In sharp contrast, the Purcell-enhanced radiative decay rate of excitons in the designed optical modulator ($\Gamma = {g_{\mathrm{cavx}}}^2/(\gamma_{\mathrm{cavr}} + \gamma_{\mathrm{cava}})$) is enhanced significantly (16.2 meV), ~ 7 times larger than its intrinsic radiative decay rate. The comparable Purcell-enhanced radiative decay rate of excitons to its non-radiative decay rate lays the foundation of efficient optical modulation. The non-perfect fitting in **a** results from the fact that the dispersion of the dielectric background of the WS_2 monolayer is not considered in the CMT model.

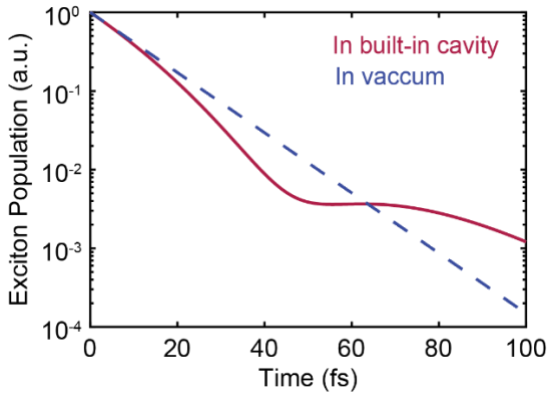

Supplementary Fig. 7 | Accelerated exciton decay process in the coupled system. The red curve shows the time evolution of the exciton decay process when the WS_2 monolayer is embedded in the metasurface cavity (i.e., the proposed modulator configuration), while the blue curve shows the case when the WS_2 monolayer is suspended in the vacuum. In the first 50 fs, the exciton decays notably faster when coupled with the metasurface cavity, indicating that the Purcell-enhanced radiative decay rate becomes comparable to the rate of other unwanted decay channels which dominate the decay process in the vacuum. Gentle wiggles in the red curve reveal that the coupled system falls into an intermediate regime between the typical weak coupling and strong coupling regime.

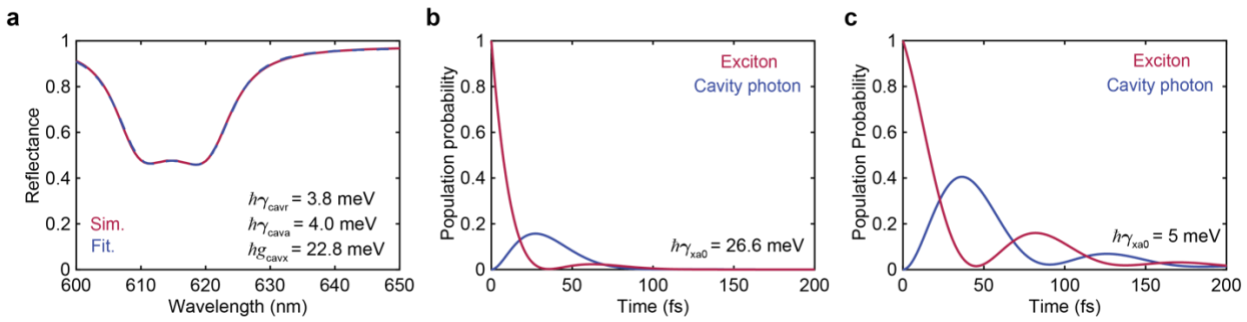

Supplementary Fig. 8 | Realizing strong coupling using a slightly different modulator design. **a,** Simulated (red) and fitted (blue) reflection spectra of the optical modulator with a 1 nm-thick gate oxide. The double-dip lineshape indicates that a strong coupling occurs. **b,** Time evolution of the coupled system that is simulated in **a**. A weak Rabi oscillation is observed. **c,** Time evolution of an optimized coupled system, where the non-radiative decay rate of the excitons is reduced to 5 meV.

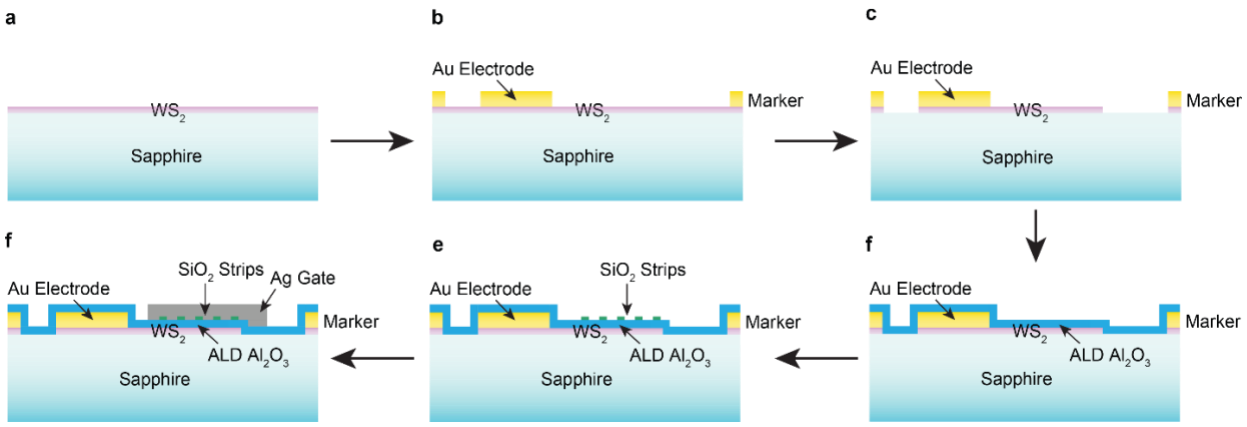

Supplementary Fig. 9 | Schematic of the fabrication process of the monolayer WS_2 free-space optical modulator. a, A piece of mm-scale WS_2 monolayer is prepared on a sapphire substrate. **b,** Au electrode and marker patterning. **c,** WS_2 monolayer pad isolation. **d,** Gate oxide deposition. **e,** SiO_2 nano-strip patterning. **f,** Ag top gate pad patterning.

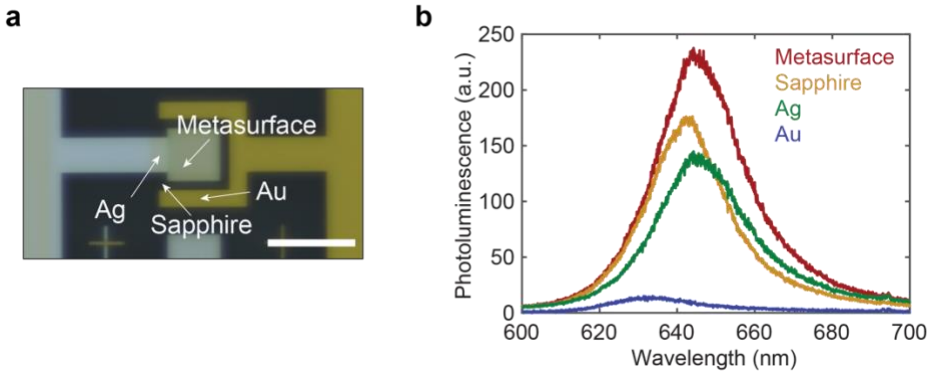

Supplementary Fig. 10 | Spectrally resolved photoluminescence measurements on the fabricated optical modulator. a, Optical image of the fabricated optical modulator. The arrows indicate the positions where we collect the photoluminescence spectra. Scale bar: 50 μm. **b,** Measured photoluminescence spectra at different positions of the fabricated optical modulator. A polarizer is inserted to only collect the TM-polarized photon emission. We find that the photoluminescence is enhanced for the WS_2 monolayer placed on top of the metasurface gate pad due to the Purcell enhancement, while the photon emission is almost killed for the WS_2 monolayer attached to the Au electrode thanks to the quenching effect. We note that a 532 nm green laser is used to pump the WS_2 monolayer in the experiment. This wavelength doesn't overlap with any optical resonance supported by the fabricated optical modulator for absorption enhancement.

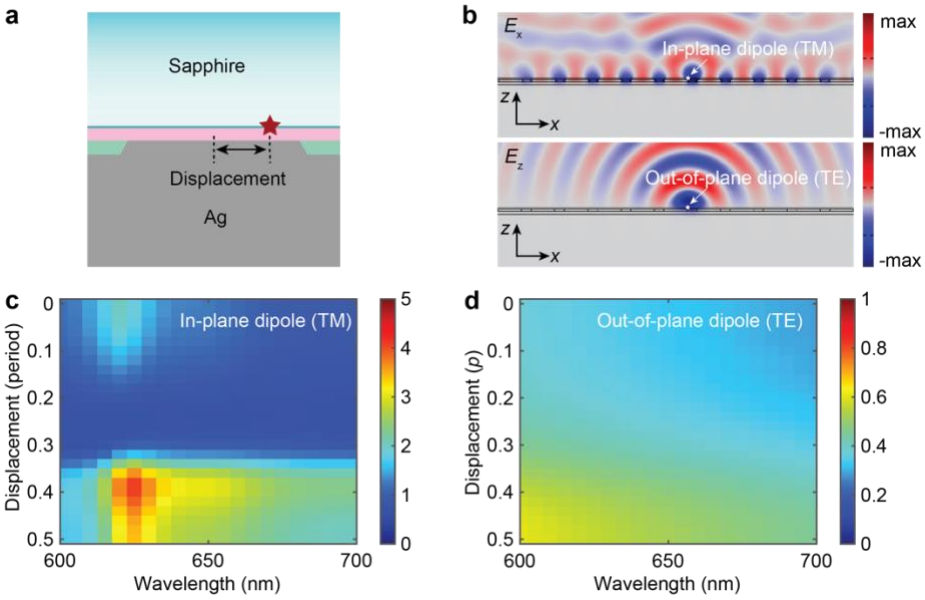

Supplementary Fig. 11 | Simulated Purcell enhancement of the exciton emission in the designed optical modulator. a, Illustration of the geometry used in the simulations. A linear electric dipole (red star) is placed in the plane of the WS_2 monolayer, displaced from the center of one specific period of the metasurface gate pad. **b,** Simulated electric-field distributions of the emission from a linear dipole (white star) placed on top of the metasurface gate pad. **c,** Simulated Purcell enhancement of an in-plane (TM) linear dipole as well as **d,** an out-of-plane (TE) linear dipole placed on top of the metasurface gate pad as a function of the dipole position and its emission wavelength. We note here that this simulation is conducted for linear dipoles in a 2D domain, and therefore may have a qualitative difference from point-dipole 3D simulations. Nevertheless, it captures the nature of the spatially dependent and polarized emission qualitatively.

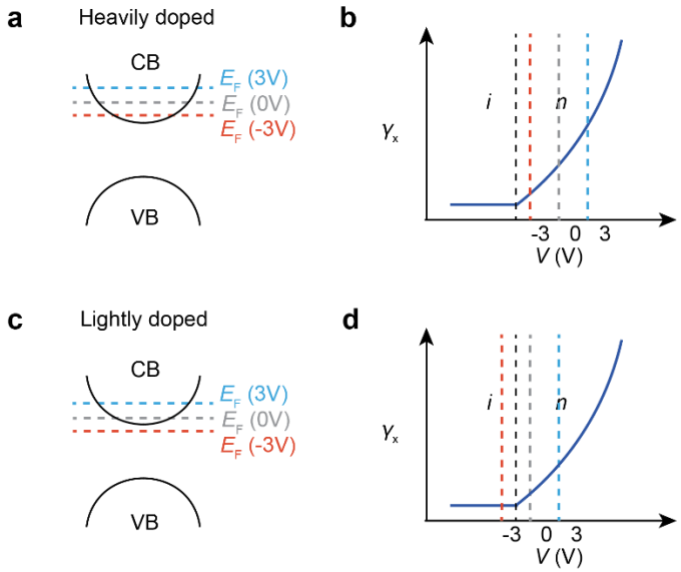

Supplementary Fig. 12 | Illustration of the Fermi-level tuning in the fabricated modulators via electrical gating. In the experiment, we find that the most efficient optical modulation is achieved from different electrical gating ranges for different samples. For example, the fabricated optical modulator exhibits an efficient modulation from -3V to 0V (Fig. 3b), while the fabricated light-field modulator is modulated most efficiently from 0V to 3V (Fig. 4f). We attribute this to the fact that the doping level of WS_2 monolayer in the as-fabricated device is different, and the reflection modulation is not linearly proportional to the change of the doping level. **a, b,** For a heavily doped WS_2 monolayer (e.g, in the fabricated optical modulator), the exciton resonance is already almost switched off (corresponding to a large exciton decay rate) before electrical gating. Therefore, additional hole injection contributes more to the optical modulation as it brings the material back to its neutral state and switches on the exciton resonance gradually. **c, d,** For a lightly doped WS_2 monolayer (e.g, in the fabricated light-field modulator), additional electron injection contributes more to the optical modulation to switch off the exciton resonance gradually. The plotted schematic of the relevant part of the WS_2 band structure and the dependence of the exciton decay rate with the gating voltage explain the above analysis graphically.

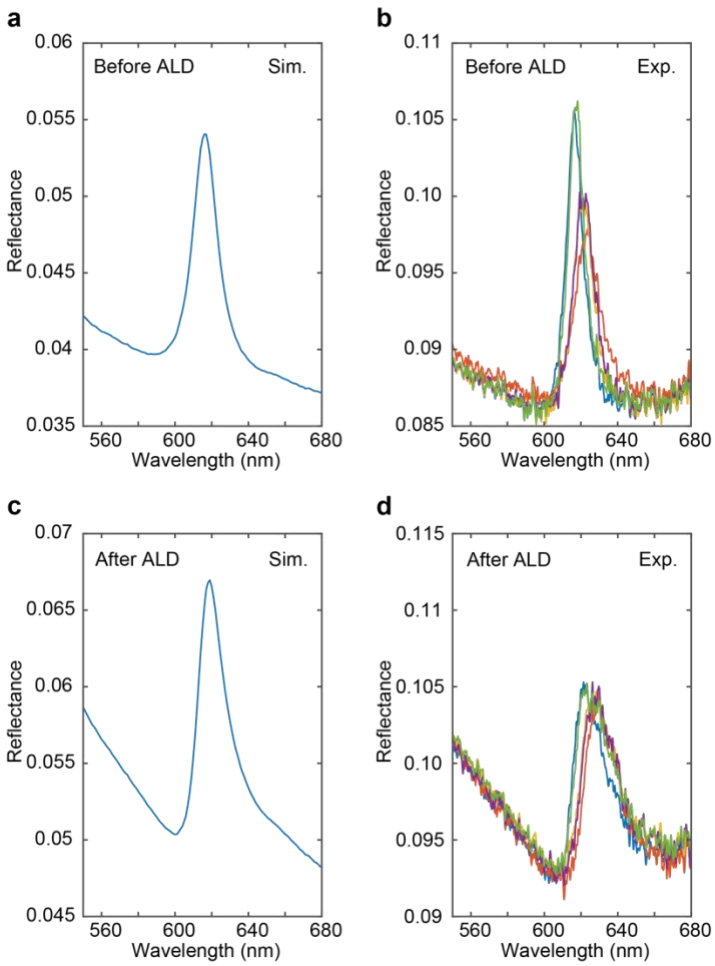

Supplementary Fig. 13 | Weaker exciton resonance observed in the fabricated modulator compared with the prime sample. a, Simulated and **b,** measured reflection spectra from five isolated WS_2 pads on a fused silica substrate before ALD Al_2O_3 encapsulation. **c,** Simulated and **d,** measured reflection spectra from the same five isolated WS_2 pads on the fused silica substrate after ALD AL_2O_3 encapsulation. We note that, the refractive index of the WS_2 monolayer used in the simulations is determined by ellipsometry measurements on a commercially available (2D Semiconductors) chemical-vapor-deposition (CVD) grown WS_2 monolayer on a sapphire substrate. As a result, it should be considered as a realistic bench marker by already taking the inhomogeneous broadening into account. Therefore, we find that the simulated reflection spectrum is consistent with the measured reflection spectra before ALD encapsulation. However, the ALD encapsulation is found to have a major negative impact on the intensity of the exciton resonance, caused by the additional doping and the dielectric and charge disorder from the ALD layer. What' more, a ~ 5 nm spectral shift of the exciton resonance is observed as well, which is attributed to the dielectric screening from the ALD layer. The overall higher reflectance observed in the measurements comes from the additional reflection from the back side of the substrate.

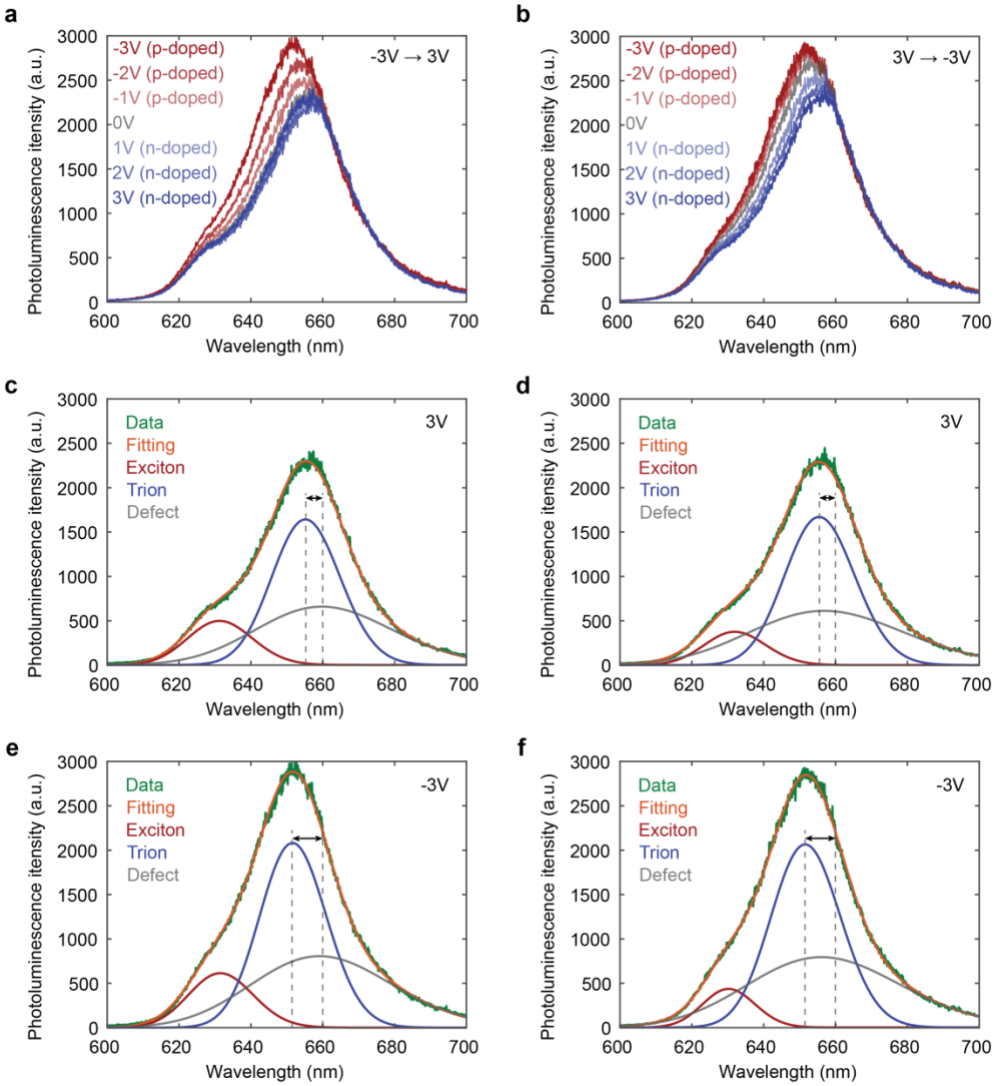

Supplementary Fig. 14 | Photoluminescence spectrum modulation of the WS_2 monolayer in the fabricated optical modulator. a, Measured photoluminescence spectra of the fabricated optical modulator when the gating voltage changes gradually from -3 V (hole injection) to 3 V (electron injection). **b,** The same measurement as **a** but the gating voltage changes from 3 V to -3 V. **c,** Gaussian fits to the measured photoluminescence in **a** at 3 V and **e,** -3 V. **d,** Gaussian fits to the measured photoluminescence in **b** at 3 V and **f,** -3 V. Three Gaussian line shapes are used to fit the measured photoluminescence spectra, corresponding to the exciton, trion, and defect-mediated recombination. We find that the photoluminescence is enhanced via hole injection by suppressing the electron-assisted non-radiative recombination. In addition, redshifts in the photoluminescence from trion recombination are observed with the increased doping level, being consistent with the previous study [13,14]. A hysteresis is also observed in the measurement, possibly due to the bias stress effect from the trapped states in the gate oxide or at the interface [15].

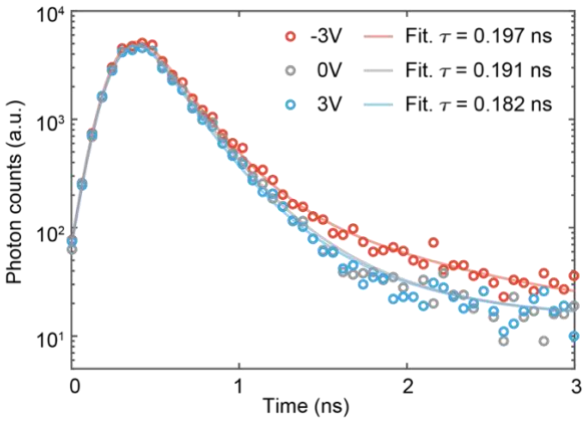

Supplementary Fig. 15 | Photoluminescence lifetime modulation of the WS_2 monolayer in the fabricated optical modulator. The figure shows the time-resolved photoluminescence decay traces with different gating voltages (shown in different colored dots). We note that due to the limited time resolution of the photodiode and the comparable instrument response function (IRF) to the decay rate of excitons, it is hard to extract the accurate lifetime of the exciton/trion emission from the WS_2 monolayer. Nevertheless, the lifetime modulation is recognizable in the measured data. We fit the measured time traces with a bi-exponential decay convolved with the IRF as shown in the different colored semi-transparent curves. We find that the lifetime of the dominant component (exciton/trion emission) decreases with electron injection, being consistent with the developed rate-equation model, while the second, much weaker component can be attributed to the defect-mediated recombination.

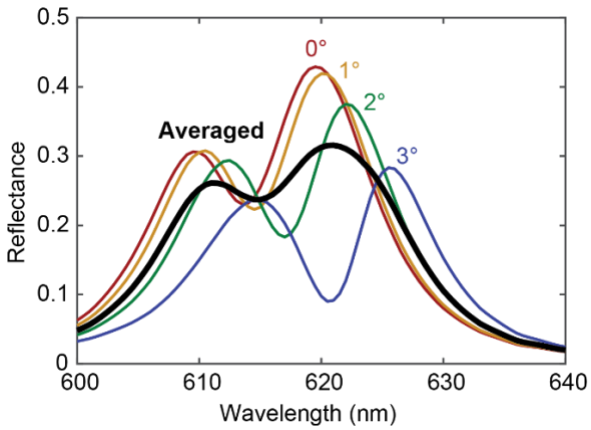

Supplementary Fig. 16 | Spectrally averaged reflection modulation with focused-beam illumination. The figure shows the simulated spectra of the absolute reflection change for the designed optical modulator under plane-wave illumination with the incident angles from 0° to 3° (different colored curves). We find that these spectra shift gradually as we increase the incident angle, originating from the dispersion of the optical mode supported by the Ag metasurface gate pad. The black curve is the spectrum of the averaged absolute reflection change under plane-wave illumination with incident angles from 0° to 3°. A relatively flat modulation plateau is found in the black curve (from 610 nm to 625 nm). This is consistent with the measured results (Fig. 3d), revealing the possibility to modulate optical beams with a certain bandwidth (~ 15 nm) as well.

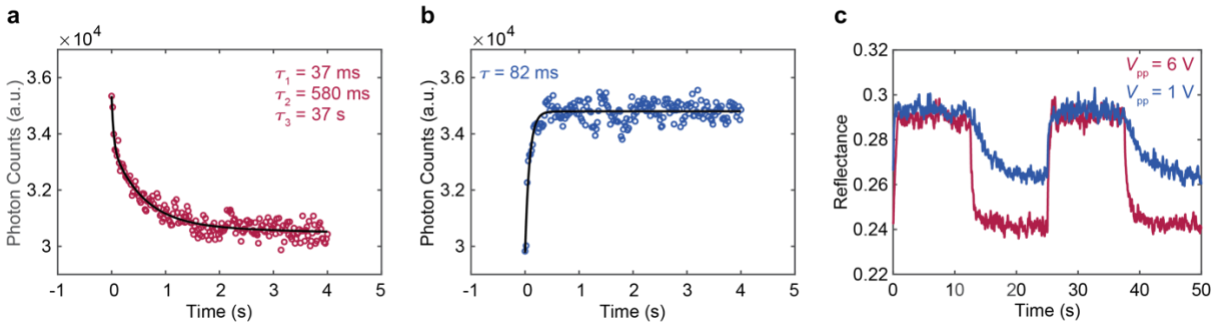

Supplementary Fig. 17 | Measured RC time constant of the fabricated optical modulator. a, Time traces of fall and **b,** rise of the reflected beam with an AC modulation. **c,** Measured reflected beam with an AC modulation with different peak-to-peak voltages. The rise time is measured to be 82 ms, while the fall time is phenomenologically fitted to a tri-exponential decay with time constants of 37 ms, 580 ms, and 37 s. We attribute this large, asymmetric, and varying RC time constant to the giant contact resistance caused by the Schottky junction at the WS_2/gold interface, as well as the large access resistance of the ungated WS_2 monolayer. The signature of the Schottky junction is further revealed by the super slow charging time when a small peak-to-peak voltage (1 V) is applied.

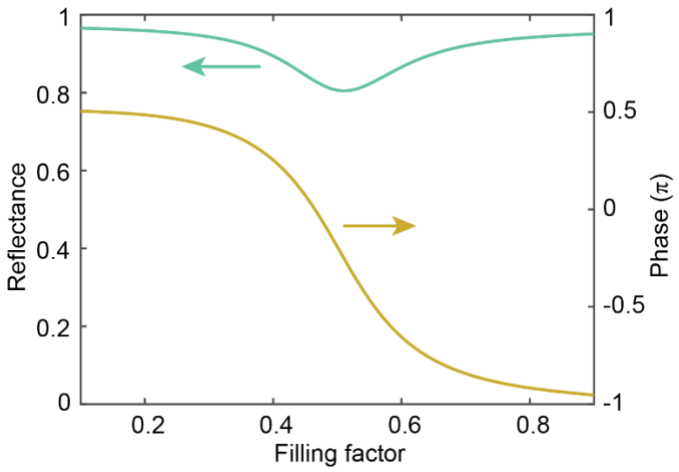

Supplementary Fig. 18 | A 2π full-phase control with an Ag metasurface gate pad. The figure shows the simulated reflectance and reflected phase of the designed light-field modulator as a function of the filling factor of the Ag bump. The exciton resonance is switched off artificially and the incident wavelength is set as 615 nm. The modulator operates in the over-coupling regime to achieve the 2π full-phase control. However, we note that the above simulations are performed under periodic conditions. Thanks to the propagation nature of surface plasmon polaritons at the metal-dielectric interface, a significant optical coupling is expected between the neighboring grooves in the metasurface gate pad. Such a coupling seriously impedes the validity of estimating local reflected phases from simulations under periodic conditions. To overcome this issue, we need to treat the entire supercell in a blazed grating as a whole to estimate its diffraction efficiency and perform a global optimization to improve it.

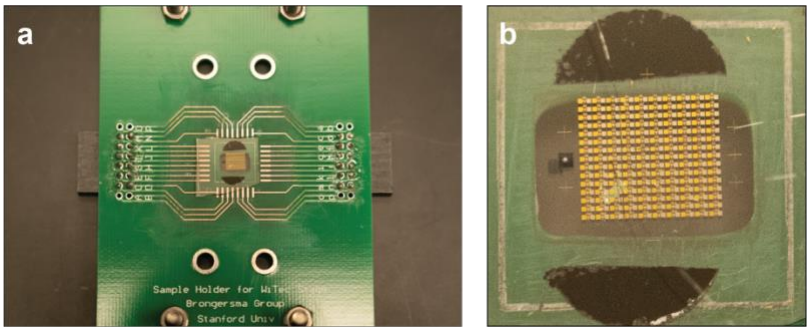

Supplementary Fig. 19 | Preparation for electrical gating experiment. a, Photograph of a homemade printed circuit board with a chip attached to it. **b,** Zoom-in image of the attached chip, where a device array consisting of 150 optical modulators is patterned. Electrodes and top gate pads are wire bonded to the printed circuit board.

References:

1. Lien, D.-H. *et al.* Electrical suppression of all nonradiative recombination pathways in monolayer semiconductors. *Science* **364**, 468–471 (2019).
2. Selig, M. *et al.* Excitonic linewidth and coherence lifetime in monolayer transition metal dichalcogenides. *Nat. Commun.* **7**, 13279 (2016).
3. Fan, S., Suh, W. & Joannopoulos, J. D. Temporal coupled-mode theory for the Fano resonance in optical resonators. *J. Opt. Soc. Am. A* **20**, 569 (2003).
4. Scuri, G. *et al.* Large Excitonic Reflectivity of Monolayer MoSe2 Encapsulated in Hexagonal Boron Nitride. *Phys. Rev. Lett.* **120**, 037402 (2018).
5. Epstein, I. *et al.* Near-Unity Light Absorption in a Monolayer WS 2 Van der Waals Heterostructure Cavity. *Nano Lett.* **20**, 3545–3552 (2020).
6. Yu, Y. *et al.* Giant Gating Tunability of Optical Refractive Index in Transition Metal Dichalcogenide Monolayers. *Nano Lett.* **17**, 3613–3618 (2017).
7. Kang, K. *et al.* High-mobility three-atom-thick semiconducting films with wafer-scale homogeneity. *Nature* **520**, 656–660 (2015).
8. Wang, J. *et al.* Dual-coupling-guided epitaxial growth of wafer-scale single-crystal WS2 monolayer on vicinal a-plane sapphire. *Nat. Nanotechnol.* **17**, 33–38 (2022).
9. Chen, T.-A. *et al.* Wafer-scale single-crystal hexagonal boron nitride monolayers on Cu (111). *Nature* **579**, 219–223 (2020).
10. Kim, S. M. *et al.* Synthesis of large-area multilayer hexagonal boron nitride for high material performance. *Nat. Commun.* **6**, 8662 (2015).
11. Kang, K. *et al.* Layer-by-layer assembly of two-dimensional materials into wafer-scale heterostructures. *Nature* **550**, 229–233 (2017).
12. Mannix, A. J. *et al.* Robotic four-dimensional pixel assembly of van der Waals solids. *Nat. Nanotechnol.* **17**, 361–366 (2022).
13. Morozov, S., Wolff, C. & Mortensen, N. A. Room-Temperature Low-Voltage Control of Excitonic Emission in Transition Metal Dichalcogenide Monolayers. *Adv. Opt. Mater.* **9**, 2101305 (2021).
14. Mak, K. F. *et al.* Tightly bound trions in monolayer MoS2. *Nat. Mater.* **12**, 207–211 (2013).
15. Datye, I. M. *et al.* Reduction of hysteresis in MoS 2 transistors using pulsed voltage measurements. *2D Mater.* **6**, 011004 (2018).